

Eruption frequency and magnitude in a geothermally active continental rift: The Bora-Baricha-Tullu Moye volcanic complex, Main Ethiopian Rift

A.Z. Tadesse^{1*}, K. Fontijn^{1,2}, A.A. Melaku³, E.F. Gebru^{3,4}, V.C. Smith⁵, E. Tomlinson⁶, D. Barfod⁷, P. Gopon^{2,8}, F. Bégué⁹, L. Caricchi⁹, P. Laha¹⁰, H. Terryn¹⁰, S. Gudbrandsson¹¹, G. Yirgu³, D. Ayalew³

¹Department of Geosciences, Environment and Society, Université libre de Bruxelles (ULB), Belgium.

²Department of Earth Sciences, University of Oxford, UK.

³School of Earth Sciences, Addis Ababa University (AAU), Ethiopia.

⁴Department of Geosciences, Université de Fribourg (UNIFR), Switzerland.

⁵Research Laboratory for Archaeology and the History of Art, University of Oxford, UK.

⁶Department of Geology, Trinity College Dublin (TCD), Ireland.

⁷NEIF Argon Isotopes, Scottish Universities Environmental Research Centre, UK.

⁸Department of Applied Geosciences and Geophysics, University of Leoben, Austria.

⁹Department of Earth Sciences, University of Geneva (UNIGE), Switzerland.

¹⁰Research Group of Electrochemical and Surface Engineering, Department of Materials and Chemistry, Vrije Universiteit Brussel (VUB), Belgium.

¹¹Reykjavik Geothermal Ltd, Iceland.

*Corresponding author: Amdemichael.Tadesse@ulb.be, amdemichaelz@gmail.com, Tel +32471309363

22

23 **Abstract**

24 Many Quaternary silicic volcanoes in the Main Ethiopian Rift pose a potential risk due to the
25 poorly known eruptive histories of the volcanoes in combination with a high population
26 density. In this study we provide new constraints on the Late Pleistocene-Holocene eruptive
27 history of the Bora-Baricha-Tullu Moye (BBTM) volcanic complex located in the central
28 portion of the Main Ethiopian Rift (MER). BBTM constitutes three main silicic edifices (i.e.
29 Bora, Baricha and Tullu Moye) and numerous smaller vents (including Oda and Werdi).
30 Tephra deposits from these vents are several centimetres to meters in thickness in currently
31 densely populated regions and where geothermal development is taking place. We present
32 new field observations in addition to physical, petrographic, geochemical and
33 geochronological data. BBTM experienced at least 27 explosive eruptions, of varying
34 magnitude, in the last ca. 100 ky. The two oldest tephra deposits in our compiled
35 stratigraphy are associated with large-magnitude, and possibly caldera-forming eruptions.
36 The youngest of these (Meki) occurred at 107.7 ± 8.8 (2 σ) ka, which makes it the youngest
37 caldera-forming eruption identified in the Central MER so far. During the post-caldera stage,
38 BBTM underwent at least 25 eruptions sourced from the Baricha (9 eruptions), Bora (3), Oda
39 (8), Werdi (3) and Tullu Moye (2) edifices. The return period of explosive activity in BBTM is
40 thus at least one moderate-to-large explosive eruption every 4000 yr. Well-exposed units
41 have estimated eruption magnitudes (M) that are 4 to 5, while smaller-scale eruptions reach
42 up to 2.5 and are exclusively preserved near the Tullu Moye vent. The tephra was dispersed
43 up to 20 km from the volcanic complex suggesting that more than one hundred thousand

people could be exposed to tephra fall and pyroclastic density current hazards from future of similar-magnitude eruptions in this area.

Key words

Bora-Baricha-Tullu Moye; Main Ethiopian Rift; tephrostratigraphy; explosive eruptions

1. Introduction

The Main Ethiopian Rift (MER) is a mature volcano-tectonic rift zone with Quaternary silicic volcanoes arranged regularly along the rift axis, and numerous small, fault-controlled mafic eruptive centres (Fig. 1). The silicic volcanoes have produced hundreds of cubic kilometres of highly evolved magmas, and many of them host large caldera depressions and geologically young (i.e. Late Pleistocene-Holocene) edifices formed in the post-caldera stage (e.g. Corbetti: Rappich et al. 2016; Aluto: Hutchison et al. 2016a, b; and Gedemsa: Peccerillo et al. 2003; Fig. 1). Many of these volcanoes pose a high-risk due to the high population density and their poorly known eruptive histories (Aspinall et al. 2011; Loughlin et al. 2015). Long repose periods (several 100 to 1000 years for some MER volcanoes; Martin-Jones et al. 2017; Fontijn et al. 2018; McNamara et al. 2018; Siegburg et al. 2018) further compromise hazard awareness and, thus, efforts to reduce or mitigate the risk (e.g. Donovan & Oppenheimer 2012). Several MER volcanoes currently show signs of geophysical unrest, primarily in the form of ground deformation detected by satellite radar interferometry (Biggs et al. 2011; Hutchison et al. 2016c; Albino & Biggs 2021). The current study focuses on one of these volcanoes (Bora-Baricha-Tullu Moye) with the aim to improve

our understanding of its eruptive history and the related hazard for neighbouring populations and socio-economic development.

The Bora-Baricha-Tullu Moye (BBTM) volcanic complex is located in the central portion of the MER (Fig. 1). Bora, Baricha and Tullu Moye are the three main silicic edifices, among several smaller ones (including Oda and Werdi, Fig. 2). At present BBTM is active and has experienced ongoing low frequency seismicity (e.g. Greenfield et al. 2019 a, b) and episodic ground deformation over at least the past decade (Biggs et al. 2011; Albino & Biggs 2021).

The earliest reconnaissance studies on the distribution of the volcanic products were performed in the 1970s (Di Paola 1972; Bizouard & Di Paola 1978) and recognised that Tullu Moye (in the east of the complex) mainly erupts comendites, and pantellerites are mainly found in the west, around Bora and Baricha. Since then, several studies have focused on the geothermal potential of the area that is 500 MWe annually (UNDP 1973; ELC 1987; Mamo 2002; Varet & Birba 2018). At the time of writing, the area is at an advanced geothermal exploration stage, with ongoing drilling operations that are mainly located on the eastern side (Tullu Moye) of the complex. The location of this significant investment project and the high population density of the area located in towns such as Meki, Alem Tena, Iteya and Assela, all within 20 km of at least one of the main volcanic edifices, motivated this volcanological study.

BBTM experienced several explosive eruptions in the past as identified from a preliminary stratigraphic sequence presented by Fontijn et al. (2018). This study builds on their previous work, providing new field observations, physical (componentry), petrographic, geochemical (glass major and trace element geochemistry), and geochronological ($^{40}\text{Ar}/^{39}\text{Ar}$ and ^{14}C) data on pyroclastic deposits across the BBTM. We establish a tepthrostratigraphic framework for

the BBTM volcanic field to constrain the frequency-magnitude relationship of the eruptive events at this active caldera system.

2. Geological Setting

The MER is an active rift zone stretching between the Afar and Turkana depressions in the East African Rift (EAR). The MER is bounded by roughly NE-SW oriented border faults separating the surrounding Eastern and Western Plateaux. The rift gradually narrows from the southern Afar depression into the MER with a minimum width of ~80 km. The southern MER boundary is considered to be located at ~5°N latitude (Balestrieri et al. 2016) where a ~300 km-wide system of basins and ranges called the Broadly Rifted Zone exists (Ebinger et al. 2000). Here, the rift zone widens and the deformation becomes more distributed.

The present-day configuration of the MER suggests the progressive narrowing of volcano-tectonic activity with time that will eventually lead to continental breakup and subsequent oceanic spreading (e.g. Ebinger & Casey 2001; Ebinger 2005; Rooney et al. 2007; Daly et al. 2008; Bastow et al. 2011). The Quaternary deformation and volcanism have mainly concentrated on the axial magmatic segments that are located along a 20 x 60 km zone (i.e. Wonji Fault Belt, WFB; Ebinger & Casey 2001; Keir et al. 2006). In these magmatic segments the younger products erupted from volcanic fissures, scoria cones and large central volcanoes are collectively known as the Wonji group (e.g. WoldeGabriel et al. 1990). This group is dominated by silicic volcanic rocks erupted from the large central volcanoes aligned along the axial zone of the MER (i.e. Corbetti, Aluto, BBTM, Gedemsa, Boku, Boset-Bericha, Kone and Fentale; Fig. 1). These volcanoes are systematically spaced (ca. 20-45 km apart), with edifices rising hundreds of meters above the MER plain. Some of these large silicic

edifices are associated with well-developed caldera structures (e.g. Kone, Gedemsa), where others have calderas that are largely concealed by post-caldera eruptive products (e.g. Aluto). The post-caldera eruptive products primarily occur as silicic tephra deposits and (obsidian) lava flows (e.g. Peccerillo et al. 2003; Hutchison et al. 2016a, b; Rapprich et al. 2016; Fontijn et al. 2018).

Volcanic products from the present-day BBTM volcanic centres, including Bora, Baricha and Tullu Moye, overlie Late Pleistocene ignimbrites that have been K-Ar dated to 1.58 ± 0.2 Ma (Table 1; WoldeGabriel et al. 1990). Three borehole wells (TG-1, TG-2 and TG-3; Fig 2) show that the BBTM subsurface geology consists of trachyte and rhyolite lava flows at the base, which are overlain by weakly to moderately compacted layers of ignimbrites and unwelded pyroclastics (Ayele et al. 2002). The rhyolite lavas thin out and the fine-grained ignimbrites become very thick (87.5 m) at TG-2. Another well (TG-4) drilled near a rhyolite dome (Adano) shows very thick (100 m) trachytic and rhyolitic lavas with variable porphyritic to fully glassy (obsidian) texture overlaying an ignimbrite similar to that observed in the rift escarpment (Ayele et al. 2002). Well TG-5 is located close to Tullu Moye volcano and incorporates very thick (90.5 m) porphyritic and scoriaceous basalt at the base. The subsurface lithologies show alteration that is likely related to the persistent hydrothermal activity in the region (Ayele et al. 2002).

The surface geology of Bora and Baricha is characterized by poorly to completely unwelded pumice and ash deposits (Di Paola 1972). Subordinate rhyolitic lavas are associated with the pyroclastics at Baricha (e.g. Di Paola 1972; ELC 1987; Ayele et al. 2002). Near Baricha, Fontijn et al. (2018) identified >7 pantelleritic pumice fall deposits alternating with poorly-

developed palaeosols. Several smaller pumice vents are located to the east of Bora and Baricha, including Werdi and Oda (Fig. 2).

Tullu Moye is situated in the intensely faulted part of the region (also known as the Salen range; Varet & Briba 2018) along the WFB, and has trachytic lavas and hydrothermally altered pyroclastic deposits. The whole rock (Bizouard & Di Paola 1978) and glass (Fontijn et al. 2018) chemical compositions indicate that Tullu Moye pumice and obsidian lava have a comenditic composition. The plain located to the NE and SW of Tullu Moye is covered by thick obsidian (at Giano and Janno/Miesa; Ayele et al. 2002) and basaltic flows and associated scoria, spatter and cinder cones. Those products erupted along fissures and conceal some of the earlier Tullu Moye tephra deposits (UNDP 1973; ELC 1987). The Giano obsidian flow (after Bizouard & Di Paola 1978) possibly erupted during historical time (ca. 1900 CE) and covers a 2.7 X 1.6 km area; though detailed accounts of the eruption or its exact age are not known (Gouin 1979).

Since the Late Cenozoic, tectonic activity in the MER caused subsidence and formed an asymmetric basin with fluvio-lacustrine sedimentation (e.g. Le Turdu et al. 1999). Today several lakes exist in this asymmetric MER floor (Fig. 1). Most of these lakes were repeatedly connected and disconnected in the Quaternary as a result of tectonic subsidence and/or lake level fluctuations (Benvenuti et al. 2002, 2013). At least two major lake expansion phases are recorded in the sediments (Benvenuti et al. 2002). The oldest “Megalake” phase occurred around the Late Pleistocene (ca. 100 ka) and is separated from a second lake level high-stand (“macrolake” phase, ca. 10 ka) by an erosional contact that resulted from prolonged low-stand and lake level fluctuations (e.g. Benvenuti et al., 2002; Le Turdu et al. 1999). The fluvio-lacustrine sediments are interbedded with volcanic (pyroclastic and

epiclastic) deposits, providing evidence for episodic volcanic activity throughout the Late Quaternary (Le Turdu et al. 1999; McNamara et al. 2018). In the northern and central portions of the MER these lacustrine sediments reach up to tens of meters of thickness (Le Turdu et al. 1999; Benvenuti et al. 2002). Subsurface geophysical investigations (e.g. Mulugeta et al. 2021) and deep boreholes (e.g. Teklemariam et al. 1996) around Aluto volcanic complex reveal lacustrine deposits that are up to 600 m in thickness.

3. Methods

Field campaigns were performed in 2015, 2017 and 2020. A total of 162 outcrops were systematically logged, and samples were collected for each stratigraphic unit from multiple sites around the volcanic complex (Fig. 2a). Pyroclastic units were correlated using a combination of field observations (including lateral tracing between outcrops), physical characteristics and chemical compositions.

Componentry analysis was performed to quantify the proportions of different particle types that occur in tephra deposits sourced from different centres across the BBTM. Eighty-five samples, each up to 2 kg, from selected tephra layers, and in some cases from different stratigraphic levels of the same deposit (e.g. base, middle and top) were dry-sieved at 1 ϕ intervals between -2 ϕ (4 mm) and 2 ϕ (0.25 mm). In each grain size fraction particles were qualitatively assigned into classes, counted and weighed. The assigned classes are: (1) Vesicular juvenile, which are unaltered to slightly altered pumiceous clasts; (2) Dense juvenile, which are poorly- to- non-vesiculated, dense and fresh volcanic glass shards; (3) Accidental dense lithics; and (4) Free crystals, which may be juvenile or xenocrystic. Each class was described qualitatively according to colour, vesicularity, vesicle size, vesicle shape,

crystallinity and type (Houghton & Wilson 1989; Cas et al. 2008). Vesicular juvenile clasts of each bed-set were qualitatively described and classified based on colour (i.e. yellow-brown, dark-grey, light grey, bluish-grey and white) and clast textures using nomenclature as per Polacci et al. (2003): expanded (extensive vesicle expansion with >90% interconnected vesicles), microvesicular (equidimensional clasts containing heterogeneous vesicles) and tube (fairly elongated to highly stretched vesicles). The lithic fragments were qualitatively described according to their levels of alteration (i.e. reddish to light brown colour) and nature (lava, obsidian and green ignimbrite). The data presented in section 4.1 is the average of all analysed grain size fractions between 4 mm and 0.25 mm (see Table 2).

Thin sections of selected pyroclastic and lava samples were prepared by TS Lab and Geoservices, Italy. Modal mineral percentages were estimated by an automated point counting method using ImageJ (Schneider et al. 2012) and the image analysis toolbox Jmicrovision 1.3.1 (Roduit 2019). At least 300 points were counted per field-of-view. To measure the areas of vesicles and solid material (groundmass (typically glassy) and crystals), each phase was segmented by manual bi-level greyscale thresholding based on the histogram of the image. Vesicle and groundmass / crystal proportions were then recalculated using the mineral area proportions in the solid phase as obtained from the point counting.

For glass chemical analysis pumice lapilli were manually crushed using an agate pestle and mortar. The crushed samples were wet-sieved at 80 μm to remove the finer clay-sized fraction that cannot be analysed and dried in an oven at 50 °C. The recovered fresh shards were cold-mounted in pre-drilled EpoFix resin discs and polished with SiC paper (grade P1200 and P2400) and diamond paste (3 and 1 micron). Back-scattered electron (BSE)

203 imaging and semi-quantitative compositional analyses were performed with a JEOL JSM-
204 IT300 scanning electron microscope fitted with an Oxford instruments SDD X-MaxN EDS
205 detector at the Department of Materials and Chemistry, Vrije Universiteit Brussel (VUB) to
206 determine suitable points for qualitative glass analysis, avoiding phenocrysts and
207 microlites. The SEM and EDS data for selected samples is displayed in the supplementary
208 material (SM-1).

209 Glass major element data was acquired by Electron Microprobe Analysis (EPMA) using a
210 JEOL JXA-8600 Superprobe (Research Laboratory for Archaeology and the History of Art,
211 University of Oxford), a JEOL 8200 (Department of Earth Sciences, University of Geneva) and
212 a CAMECA SX5-FE (Department of Earth Sciences, University of Oxford). On all three
213 instruments, the same analytical protocol was used. Analyses were conducted on carbon-
214 coated polished grain mounts using an accelerating voltage of 15 kV, a low beam current (6
215 nA) and a defocused beam of 10 μm . For samples with smaller glass areas, a 4 nA beam
216 current and a probe diameter of 6 μm were used. Counting times on the peak were set to 30
217 seconds (Si, Al, Ti, Ca) and 60 seconds (P, Mg, Mn, Fe). Due to Na and K mobility and loss
218 issues, Na and K were analysed first on each spectrometer, and were measured with a short
219 peak count time of 12 seconds. The background count times at the high and low background
220 where half of the peak count time. The instruments were calibrated with a suite of
221 appropriate mineral standards, listed on supplementary material (SM-2). Analysis of
222 secondary glass standards (ATHO-G, StHs6/80-G and MLB-3-G; Jochum et al. 2006) was used
223 to regularly verify the calibration. The secondary standards analytical precision is typically <
224 $\pm 4\%$ relative standard deviation (RSD) for most major elements, except for the low
225 abundance elements such as Ti ($\pm 8\%$), Mn ($\pm 30\%$) and P ($\pm 38\%$). At least 20 individual
226 points were analysed per sample. Only analyses with totals above 92 wt% were considered

227 reliable, and data were normalized to 100% before being plotted (Frogatt 1983; Lowe 2011).
228 A representative set of analyses are presented in Table 3; the full data set is available in
229 supplementary material (SM-2).

230 Trace element analyses of glass shards for some tephra units were conducted by Laser
231 Ablation – Inductively Coupled Plasma – Mass Spectrometry (LA-ICP-MS) at the iCrag
232 laboratory, Trinity College Dublin (TCD) using a Teledyne Photon Machine G2 193 nm
233 excimer laser ablation system with a two-volume Helex cell coupled to a Thermo Scientific
234 iCAPQ ICP-MS. We used a spot size of 30 μm , a repetition rate of 5 Hz with a 35 s acquisition
235 time with 30 s for washout between samples. Concentrations were calibrated using a
236 NIST612 glass standard (using the composition reported by Jochum et al. 2011) with ^{29}Si as
237 the internal standard. During the measurement, the calibration was verified using MPI-DING
238 glasses (ATHO-G and StHs6/80-G; Jochum et al. 2006). Data reduction was undertaken using
239 Iolite 3.4. The secondary standards trace element analysis precision is typically $\leq 11\%$ except
240 for Rb, Sr, Y and Nb ($\leq 7\%$) in RSD.

241 Two pumice samples (MER149A and MER147-2D) were prepared at the Department of
242 Earth Sciences, University of Oxford for single-crystal $^{40}\text{Ar}/^{39}\text{Ar}$ dating. The samples were
243 crushed and sieved, and 250-500 μm size fractions were recovered. These fractions were
244 cleaned in distilled water in an ultrasonic bath, dried in an oven at 50 $^{\circ}\text{C}$ and passed multiple
245 times through a Frantz Isodynamic magnetic separator to concentrate sanidine crystals. The
246 sanidine concentrates were leached in 5% HF to remove any adhering glass, and examined
247 under a binocular microscope to collect pristine, inclusion-free, grains. Dating was
248 performed at the NEIF Argon Isotope Laboratory at the Scottish Universities Environment
249 Research Centre (SUERC), University of Glasgow. Samples and neutron flux monitors were

packaged in aluminium discs and stacked in quartz tubes for later reconstruction of neutron flux gradients. The sample package was irradiated in the Oregon State University reactor, Cd-shielded facility. Alder Creek sanidine (1.1891 ± 0.0008 (1σ) Ma; Niespolo et al. 2017) was used to monitor ^{39}Ar production and establish neutron flux values (J) for samples. Ar isotopic measurement was performed on a MAP-215-50 instrument, single-collector mass spectrometer using an electron multiplier collector. Blanks were analysed at the start and in between every run. Mass discrimination during the sample run was monitored and calibrated by analysis of air standards. Mass discrimination, nucleogenic interference and atmospheric contamination were corrected using MassSpec software (version 8.058). Ages were calculated using the decay constant factors after Renne et al. (2011) and yields an age of 107.7 ± 8.8 ka (MER149A) and 87 ± 16 ka (MER147-2D) with 2σ uncertainty.

One sample of charcoal embedded within a BBTM tephra deposit was sampled for accelerator mass spectrometry radiocarbon dating. The conventional age of 871 ± 24 ^{14}C yr BP was calibrated using Oxcal 4.4 (Bronk Ramsey 2009) using the IntCal20 calibration curve (Reimer et al. 2020). The calibrated radiocarbon age gives an age of 1190 ± 36 cal yrs BP (760 ± 36 CE) with a 95.4% probability interval.

After constraining the tephrostratigraphy, the tephra fall volume of individual deposits was estimated for some major eruptions by manually constructing isopachs, based on 4 to 10 data points. We calculated the minimum bulk deposit volumes using the Pyle (1989) and Legros (2000) method.

4. Results

4.1. Field stratigraphy and Geochronology

We identify 27 individual volcanic deposits that are all interpreted to be the products of separate explosive eruptions. The deposits are distinguished based on lithological (e.g. componentry, clast textures, glass geochemistry) and depositional characteristics. Most units are correlated at a local/sub-regional scale based on field and laboratory data, except for some of them (at least seven; section 4.1.8). In the following descriptions, the deposits are categorized on their interpreted source vent/area and described from the oldest to youngest for each category. Based on the distance from the vent area, the outcrops are defined as very proximal (<5 km from the vent), proximal (5-10 km), medial (10-30 km) and distal (>30 km). The identified stratigraphic units are labelled in systematic stratigraphic order from base to top, starting with two letters that represent the source vent (e.g. the basal pumice unit from Baricha is Ba-P1 and is overlain by Ba-P2). The location of each section is presented on Figure 2 and in supplementary material (SM-3). The overview of the stratigraphic record and unit correlations is shown on Figure 3. Key images and description of representative outcrops (Fig. 4; SM-3), componentry, and petrography (Fig. 5; SM-4) are also displayed on separate figures and all the data is included in the supplementary material. Table 2 represents the main characteristics of all BBTM deposits; descriptions of widely dispersed eruptive units (i.e. major deposits, correlated across at least 5 sections) are given below. In these descriptions, we simply mention the chemical composition of the units to support the correlations, but more details of the geochemistry are given in Section 4.2.

4.1.1. Suke Deposit

The Suke deposit is the oldest pyroclastic BBTM unit identified in the region. The base of the deposit is not observed, but the unit is overlain by a succession of Meki pumice (section

4.1.2) and porphyritic basaltic lava in different sites. Glass compositions of the Suke unit are pantelleritic. The deposit is exposed at only a few locations (MER253 and MER367) in the area of Suke, along a deep gully in the north-central part of the complex (Fig. 2). It has a maximum thickness of 6 m at Suke (MER253) and is very poorly sorted, clast-supported, and fine depleted, with bombs and lithic blocks up to 1 m in diameter of aphyric obsidian, dense pumice and altered lava (Fig. 3a; Fig. 4). About 3 km east of the type locality, in section MER367, the fine-grained component (<2 mm) with both pumiceous and lithic material becomes dominant (>50%). The pumice is light to dark grey and very crystal poor with only <1% of aenigmatite and no other visible crystals. The depositional characteristics indicate that the Suke deposit is an ignimbrite with a lithic lag breccia facies in proximal section MER253, and representative of pyroclastic density currents (PDCs) formed during a caldera-forming eruption. The absence of any datable material (e.g. sanidine phenocrysts) prevents us from constraining the absolute age of the Suke ignimbrite.

4.1.2. Meki Deposit (107.7 ± 8.8 ka)

The Meki deposit is exposed in four places around the town of Meki (Fig. 2). It is also underlain by the Suke deposit and overlain by tephra deposits sourced from Baricha (cf. Section 5.1.3) in the Suke locality (MER253; Fig. 3a). At this latter location, the Meki deposit is separated from both under- and overlaying units by weakly developed palaeosols. The largest outcrop exposes >20 m of pyroclastic deposits in a quarry site near the Ziway-Meki road (MER149 and MER326). There, the basal portion (up to 3 m exposed) of the sequence is a well-sorted, massive, fine to coarse pumice lapilli breccia that is free of accidental lithics. In this lower part of the quarry, at ca. 1660 m asl, distinct sub-horizontal brown staining on

319 the pumice surface is observed over a thickness of ca. 1 m in the MER149 and MER326
320 outcrops. The middle portion of the deposit is characterised by alternations of well-sorted
321 and poorly sorted fine lapilli breccia units that range between 10 and 90 cm in thickness.
322 The poorly sorted part of the deposit does not maintain a consistent local thickness and
323 becomes very thick (~13 m) in a section west of Meki town (MER327; Fig. 2a). At this section
324 the deposit is poorly sorted, displaying a variety of lenticular and wavy bedding, horizontal
325 laminations (alternation of mm-scale fine ash and lapilli layers), and in places mm-scale sub-
326 parallel to low-angle cross-bedding, with sub-rounded pumice lapilli in a fine ash matrix. The
327 upper ~8 m of the Meki deposit is, again, a massive, well-sorted and lithic-free pumice lapilli
328 breccia with ca. 10% of expanded pumice clasts. The deposit from the Meki section (i.e.
329 MER149) is virtually free of lithics and contains 80-95% pumice clasts (45-90%
330 microvesicular-light grey and ≤40% expanded-dark grey coloured pumice) and 5-20% free
331 crystals (alkali feldspar and aenigmatite) in the finer fractions below 1 mm. The pumice
332 clasts are highly vesicular (ca. 70-75% vesicularity), almost aphyric with ca. 1% phenocrysts
333 of alkali feldspar and aenigmatite, within a microlite-free groundmass. The Meki deposit has
334 distinct pantellerite glass compositions (section 4.2) relative to the Suke deposit, allowing
335 the correlation between the two main sequences in the area of Meki (west of the BBTM
336 complex) and Suke (central part; Fig. 2). At the Suke section, the Meki deposit is represented
337 by three stratigraphic horizons that show coarse lapilli at the base and matrix-dominated
338 massive beds at the top. The lack of an erosive surface or palaeosol between these horizons
339 suggests there was not a significant time gap between their depositions. Both in Suke and
340 Meki, we interpret the lower and upper portions of the deposit as a tephra fall, and the
341 middle part as a diluted PDC that is also interbedded with minor tephra falls. Sanidine

crystals from the lower part of the deposit were dated by $^{40}\text{Ar}/^{39}\text{Ar}$ to 107.7 ± 8.8 ka (Table 1).

4.1.3. Baricha Sequence

The Baricha pyroclastic deposits are relatively widely dispersed to the West and well preserved in different stratigraphic sections. Some major units (i.e. well dispersed; Ba-P3 to Ba-P7) are observed in up to 25 different outcrops that extend 20 km from the summit of Baricha. The Baricha tephra sequence is stratigraphically younger than the Meki deposit, and the deposits commonly have lithics and a small proportion of expanded pumice lapilli. A deep gully (MER147) near Baricha exposes >9 distinct pantelleritic stratigraphic units (Fig. 3a). These units are separated by well-developed, 5 to >20 cm thick palaeosols. Other sections (e.g. MER205, MER301-3 and MER324) expose 6-8 individual deposits that can be correlated with the Baricha type section (MER147). Altogether, there are 5 major and 4 minor eruption deposits attributed to Baricha and sorted from oldest (Ba-P1) to youngest (Ba-P9) in Table 2. The major units are described in further detail here.

Ba-P3 is the oldest major Baricha deposit identified in a few proximal sections. A maximum thickness of ca. 3 m is observed in a section (MER205) located 4.5 km west from the summit. The basal 5-10 cm of the unit is composed of poorly sorted, well-indurated fine ash and accretionary lapilli. Above the bottom ash horizon, the deposit appears as a light grey coloured pumice lapilli breccia, that is well sorted and with massive to cm-scale crude bedding. The upper portion contains occasional pumice bombs (~15 cm) embedded in a sandy to silty cream-coloured horizon that is much more matrix-rich than the lower half of the deposit. The componentry of the middle portion of Ba-P3 shows 80-90% pumice clasts

(microvesicular), $\leq 20\%$ free crystals in the finer fractions (feldspar, aenigmatite and orthopyroxene) below 1 mm and $< 1\%$ lithics (crystal-rich obsidian). The pumice clasts are highly vesicular (ca. 65% vesicularity), moderately phyrlic with ca. 6% phenocrysts of alkali feldspar, aenigmatite and orthopyroxene in a glassy groundmass. We interpret the ash unit with accretionary lapilli and middle section of Ba-P3 formed by tephra fall and the upper portion, more matrix-rich, as the result of pedogenesis.

Above Ba-P3, a tripartite Baricha unit (Ba-P4) is exposed in different outcrops with a maximum total thickness of 3 m. The lower meter of the deposit comprises cm-scale alternations of fine lapilli and a yellowish ash bed. The rest of the deposit is massive and contains occasional pumice bombs of ~ 20 cm diameter in very proximal outcrops. The massive portion of the unit overlies a subtly normally graded 30 cm thick subunit; and it is composed of a clast-supported, poorly sorted, very coarse lapilli breccia. The componentry of the massive portion shows 45-80% pumice clasts (45-75% microvesicular, $< 5\%$ expanded and $\leq 1\%$ tube pumice), 10-35% free crystals (feldspar, aenigmatite, amphibole and Fe-Ti oxides) in the finer fractions and $\leq 10\%$ lithics (crystal-rich obsidian, altered lava and ignimbrite). The pumice clasts are moderately vesicular (65% vesicularity), and almost aphyric, with $< 1\%$ phenocrysts of alkali feldspar and aenigmatite, in a microlite-poor groundmass. The depositional characteristics indicate that the Ba-P4 deposit is a fallout tephra.

Ba-P5 is a widespread deposit identified to the West of Baricha. It is preserved in both proximal and medial outcrops, with a maximum thickness of 2.7 m. The unit is typically lithic-rich at the base and shows a gradual decrease in lithic proportion and other facies variations upwards in the stratigraphy. The bottom and top-third portions of the unit are

388 massive while the middle part shows cm-to-dm-scale diffuse bedding of generally well
389 sorted pumice lapilli breccia. In medial outcrops (e.g., MER229 and MER325), the deposit
390 shows two subunits with poorly developed normal grading. The componentry shows that
391 Ba-P5 contains 55-75% pumice clasts (55-75% microvesicular, $\leq 20\%$ expanded and $\leq 1\%$ tube
392 pumice), 5-40% free crystals (feldspar, aenigmatite, pyroxene, amphibole and Fe-Ti oxides)
393 in the finer fractions and $\leq 5\%$ lithics (crystal-rich obsidian, altered lava and ignimbrite). The
394 pumice clasts are moderately vesicular (50-65% vesicularity) with $< 10\%$ phenocrysts of alkali
395 feldspar, aenigmatite, orthopyroxene and amphibole, and a glassy groundmass. The Ba-P5
396 tephra deposit is interpreted as a fallout tephra unit. A bulk sample of this unit was
397 collected at section MER147 for single-crystal (alkali feldspar) $^{40}\text{Ar}/^{39}\text{Ar}$ dating, and yields an
398 age of 87 ± 16 (2 σ) ka (Table 1).

399 Ba-P6 is a well-preserved Baricha deposit overlying Ba-P5 and separated from it by a
400 palaeosol. A maximum thickness of ~ 4 m is measured in a proximal gully section (MER302).
401 In most outcrops (e.g. MER205 and MER302), Ba-P6 shows dm-scaled multiple horizons of
402 well-sorted coarse to fine pumice lapilli with abrupt grain size transitions. The componentry
403 shows that Ba-P6 is almost lithic-free ($\leq 2\%$ of crystal rich obsidian, altered lava and
404 ignimbrite) and contains 50-70% pumice clasts (50-70% microvesicular and $< 10\%$ expanded
405 pumice) and ca. 30% free crystals (feldspar, aenigmatite, amphibole and Fe-Ti oxides) in the
406 finer fractions below 1 mm. The pumice clasts are moderately vesicular (50% vesicularity),
407 with $< 10\%$ phenocrysts of alkali feldspar, aenigmatite and amphibole, set in a glassy
408 groundmass. The depositional characteristics indicate that the Ba-P6 deposit is a tephra fall
409 deposit.

Ba-P7 is a light grey pumice deposit confirmed in 15 different stratigraphic sections. The unit is 5 m thick at 4 km distance from the summit (MER205). The bottom of Ba-P7 is a matrix-supported and cream-coloured pyroclastic deposit in medial outcrops (at ~15 km distance from the source) and a fallout unit in proximal outcrops. The main part of the Ba-P7 unit is diffusely dm-scale bedded, but overall normally graded and poorly sorted pumice lapilli breccia. In the upper half of the unit, pumice bombs up to 10-15 cm diameter are present. The componentry shows that Ba-P7 is almost lithic-free ($\leq 2\%$ of crystal rich obsidian, altered lava and ignimbrite) and contains 65-90% pumice clasts (65-85% microvesicular, $\leq 2\%$ expanded and $\leq 2\%$ tube pumice) and 5-30% free crystals (feldspar, aenigmatite and Fe-Ti oxides) in the finer fractions. The pumice clasts are moderately to highly vesicular (50-55% vesicularity), and almost aphyric with $< 1\%$ phenocrysts of alkali feldspar and aenigmatite in a glassy groundmass. We interpret Ba-P7 as a PDC deposit (in medial outcrops) overlain by a tephra fall.

The youngest Baricha deposit found, Ba-P9, is a minor unit underlain by a cream-coloured, matrix-supported and undulatory bedded horizon that is interpreted as a PDC deposit. In outcrop MER308 a piece of black, friable charcoal was recovered from the upper part of this PDC deposit. A radiocarbon date of the charcoal yields an age of 1190 ± 36 cal yr BP (760 ± 36 CE).

In summary, at Baricha, we identify in total seven pumice fall deposits (Ba-P1, Ba-P3 to Ba-P8) and another two composite deposits that have both tephra fall and PDC units (Ba-P2 and Ba-P9; Table 2).

4.1.4. Oda Sequence

A sequence of pyroclastic deposits is exposed in the vicinity of the Oda crater and attributed to this centre. Oda has a well-developed 0.9 x 0.78 km crater partially filled by a small lake (Fig. 2a). The stratigraphic section to the SE of the summit crater (MER336) displays 8 different units with pantellerite-comendite glass compositions (Fig. 3). The tephra deposits are generally poorly preserved in medial and distal sites (>10 km). Two major (Od-P4 and Od-P5) and five minor units are assigned to Oda, each of them separated by poorly to well-developed palaeosols (Table 2).

Od-P4 is a pumice lapilli breccia deposit with cm-scale bedding and normal grading within each bed set in the bottom portion before becoming massive in the top ~30 cm. A maximum thickness of 3 m is observed in MER336. In several sections (e.g. MER231), the bottom 10-30 cm is marked by a lithic-rich poorly sorted ash-dominated horizon (i.e. tuff). The componentry shows that Od-P4 contains 60-80% pumice clasts (60-80% microvesicular and ≤1% tube pumice), ≤25% lithics (hydrothermally altered lava, glassy obsidian and ignimbrite) and 10-20% free crystals (feldspar, aenigmatite and Fe-Ti oxides) in the fractions below 1 mm. The pumice clasts are moderately to highly vesicular (55-65% vesicularity), and sparsely aphyric with ≤3% phenocrysts of alkali feldspar, clinopyroxene, amphibole and aenigmatite in a glassy to microlite-poor groundmass. The mineralogy of the microlites is similar to that of the phenocrysts. Od-P4 is interpreted as a PDC deposit overlain by a tephra fall.

Above Od-P4, a relatively well-preserved deposit (Od-P5) is exposed. Od-P5 is 3.5 m thick at Oda's flank and still ≥40 cm at 6 km distance (MER237) from the volcanic centre. The unit is characterised by a massive, fine pumice lapilli breccia, that is poorly sorted, lithic-rich and comprises few distinctly larger pumice clasts (~3.5 cm). The componentry shows that Od-P5 is lithic-poor (≤3% of hydrothermally altered lava and glassy obsidian) and contains 60-70%

pumice clasts (60-70% microvesicular and $\leq 1\%$ tube pumice) and 5-35% free crystals (feldspar, quartz, aenigmatite, pyroxene, amphibole and Fe-Ti oxides) in the finer fractions. The depositional characteristics indicate that Od-P5 is a tephra fall deposit.

4.1.5. Bora Sequence

Bora deposits are generally poorly preserved and found in the south western part of the BBTM complex. A deep gully (MER231) located at 11 km southwest of the Bora edifice exposes two major and one minor deposit with pantelleritic-comenditic compositions (Table 2, Fig. 4d). The pyroclastic deposits can be correlated with outcrops that extend to at least 14 km distance from the summit. The Bora sequence lies entirely on top of the Oda sequence and can be distinguished from the latter by its lithic-poor nature and rare hydrothermally altered lithics.

Bo-P2 is exposed in only a few proximal outcrops. The unit is a cm-scale bedded, well-sorted pumice lapilli breccia, and contains occasional pumice bombs (~15 cm in diameter). The deposit appears light grey at the base, and gradually progresses to a cream-coloured, lenticular-bedded, poorly sorted unit with sub-rounded pyroclasts towards the top. A maximum thickness of 2.5 m is observed in outcrop (MER231) located 11 km from the vent. The componentry of Bo-P2 shows 60% pumice (60% microvesicular and 1% tube pumice), $\leq 15\%$ free crystals (feldspar, quartz and Fe-Ti oxides) in the finer fractions and $< 8\%$ lithics (hydrothermally altered lava, glassy obsidian and ignimbrite). The pumice clasts are entirely aphyric and moderately vesicular (ca. 60% vesicularity). We interpret the lower half portion of Bo-P2 to be formed by tephra fall and the upper portion to result from the main unit's weathering.

Bo-P3 is a relatively widespread Bora deposit. The unit is an entirely massive, poorly sorted coarse pumice lapilli breccia. The maximum thickness of the deposit is 3 m and thins out to a minimum of 65-70 cm in medial outcrops at 13 km distance from the summit. The componentry of Bo-P3 shows it to be almost lithic-free ($\leq 1\%$ altered lava and glassy obsidian), and contain 90% pumice (80% microvesicular, 5% expanded and 3% tube pumice) and 5% free crystals (feldspar, aenigmatite, pyroxene and Fe-Ti oxides) mainly concentrated in the finer fractions. The pumice clasts are almost aphyric ($< 0.5\%$ alkali feldspar, aenigmatite and orthopyroxene), moderately to highly vesicular (45-75% vesicularity), and have a glassy groundmass. The depositional characteristics suggest that Bo-P3 is a pyroclastic fall deposit.

4.1.6. Werdi Sequence

Werde deposits are exposed in a few outcrops located in the central and northern parts of the volcanic complex. A gully section (MER309; Fig. 4e) located in the vicinity of the southern Lake Koka shore provides an apparently near complete overview of the Werdi sequence. At MER309 three Werdi units, 2 major (Wd-P1 and Wd-P2) and 1 minor (Wd-P3; Table 2), are observed. The Werdi sequence overlies the Suke deposits and is separated from it by well-developed palaeosols. The Werdi deposits are easily identified by the bluish-grey colour of the pumice clasts and pantelleritic-comenditic compositions.

Wd-P1 sits stratigraphically above the Suke deposit (MER309) and an obsidian lava flow (MER246). The unit is bedded at the cm-scale, poorly sorted, lithic-poor and composed of coarse ash to pumice lapilli. Wd-P1 has a maximum thickness of 15 m and contains occasional pumice bombs (~ 10 cm) in very proximal outcrops. Wd-P1 contains ca. 83%

bluish-grey pumice (microvesicular), ca. 10% lithics (hydrothermally altered lava and crystal-rich obsidian), and ca. 5% free crystals (feldspar, aenigmatite, pyroxene and amphibole) in the grain size fractions below 4 mm. Wd-P1 likely originates from a tephra fall.

Wd-P1 is overlain by another 35 cm thick Werdi unit (i.e. Wd-P2) in the MER309 outcrop. In outcrop MER246, Wd-P2 is underlain by crystal-rich obsidian lava. The unit appears as a lithic-poor, well-sorted and massive coarse pumice lapilli breccia. In section MER245 the top part of this unit shows normal grading. The componentry of Wd-P2 shows it to be almost lithic-free (<5% altered lava, glassy obsidian and ignimbrite), with ca. 70% bluish-grey pumice (microvesicular) and ca. 20% free crystals (feldspar, aenigmatite and Fe-Ti oxides) in the finer fractions. The pumice clasts are almost aphyric (ca. 1% alkali feldspar and aenigmatite), moderately vesicular (50% vesicularity), and have a glassy groundmass. The depositional characteristics indicate that Wd-P2 represents a pyroclastic fall.

4.1.7. Tullu Moya Sequence

Tullu Moya deposits are exposed in the heavily faulted eastern zone of the volcanic complex. Two different Tullu Moya units are identified above well-developed palaeosols in most outcrops. Both units are characterised by their distinct white pumice clasts of comenditic composition. TM-P2 is the youngest and main Tullu Moya deposit that overlies TM-P1 (Table 2). The two units are separated by a palaeosol (MER152), but in some proximal outcrops an 80 cm thick scoria lapilli (interpreted as a fall) deposit is interbedded between the two pumice horizons. TM-P2 is widespread to the West and has a maximum thickness of 2 m in proximal outcrops (e.g. MER240). TM-P2 is a massive, poorly sorted pumice lapilli breccia, and contains occasional pumice bombs (up to 15 cm). The deposit is

almost lithic-free (<3% hydrothermally altered lava and glassy obsidian), and contains ca. 70-100% white pumice (70-100% microvesicular, $\leq 1\%$ expanded and $\leq 1\%$ tube pumice) and $\leq 20\%$ free crystals (feldspar, pyroxene, amphibole and Fe-Ti oxides) in the finer fractions. The pumice clasts are almost aphyric (ca. 2% alkali feldspar, clinopyroxene and amphibole), moderately vesicular (60% vesicularity), and have a glassy groundmass.

4.1.8. Additional deposits

Besides the well-dispersed BBTM tephra deposits described in sections 4.1.1 to 4.1.7, a significant number of deposits are found in single outcrops without having a correlative in other sites. Most of these deposits are exposed on the flanks of monogenetic pumice cones. At least 11 separate vent / cones are identified around the larger edifices such as Bora, Baricha and Tullu Moye (Fig. 2a). These are interpreted as pumice cones which are also common at Aluto volcano (e.g. Clarke et al. 2020). The maximum thickness of the deposits ranges from <1 m to 8 m. These deposits are characterised by massive, poorly sorted pumice lapilli breccia with occasional pumice bombs (up to 8 cm in diameter) and expanded pumice clasts. The deposits identified at outcrops MER209 and MER150 shows an alternation of tephra layers with relative variations of sorting and stratification. The lab-based componentry analysis shows that these deposits contain 70-95% pumice clasts (60-90% microvesicular, $\leq 10\%$ expanded and <10% tube pumice), <25% lithics (altered lava, glassy obsidian and ignimbrite) and <20% free crystals (feldspar, quartz, aenigmatite and Fe-Ti oxides) in the finer fractions. The pumice clasts are rhyolitic in composition, moderately vesicular (ca. 35-60% vesicularity) and almost aphyric (<3%).

In addition to these units attributed to pumice cones, there are some other deposits observed in the BBTM volcanic complex that also have no correlatives. At least seven tephra deposits are identified in the regions around Baricha, Oda and Tullu Moye. At MER201, near the Baricha edifice, two massive pumice lapilli breccia layers have thicknesses of 1.3 m and ~2 m, but have not been identified elsewhere. At section MER 237, three relatively thin (max. 40 cm), massive, lithic-poor fine lapilli breccia units alternate with a reworked pyroclastic deposit. In the eastern rift escarpment, at MER 385, ~6 km E of Tullu Moye, two tephra layers with pantellerite-comendite compositions are found. The field data and componentry of these deposits are distinct from those of any BBTM major units.

4.2. Glass chemistry

4.2.1. Major element composition

Major element glass compositions of selected proximal, medial and distal tephra (pumice) deposits from the BBTM region reveal that the parental melts consistently have alkali-rich rhyolite compositions (Fig. 6a). The average major element compositions of the selected tephra deposits are presented in Table 3, with the full dataset in Supplementary information (SM-2). All compositions are peralkaline and are classified as either pantellerite or comendite (Fig. 6b). The latter composition is characteristic of Tullu Moye tephra only, whereas all deposits from Baricha, Suke and Meki are entirely pantelleritic. The glass compositions of Oda, Werdi and Bora tephra deposits, straddle the comendite-pantellerite boundary (Fig. 6b). Except for the distinct comenditic Tullu Moye glasses, all BBTM glass major element compositions overlap with those of Aluto, Corbetti and Gedemsa tephra deposits (Fig. 6, 7; Martin-Jones et al. 2017; Fontijn et al. 2018; McNamara et al. 2018).

Each pantelleritic deposit has a tight homogeneous composition within the larger pantellerite cluster (70.1-77.9 wt% SiO₂, 6.0-14.8 wt% TA; 7.6-11.7 wt% Al₂O₃, 4.3-7.3 wt% FeO). However, different deposits may overlap in composition, complicating correlations based on major element glass composition alone. In general, Baricha deposits tend to have the highest Total Alkali and FeO contents and are also distinct in other major element contents, e.g., TiO₂ (Fig. 7b). Meki and Suke tephra predominantly have glass compositions with a higher TiO₂ (>0.23 wt%) and CaO (>0.2 wt%) content relative to those of Baricha. Meki and Suke are also distinguished from each other, especially by their Al₂O₃ and FeO contents (Fig. 6b, 7a-d). There are no discernible chemical differences between the individual Baricha tephra units.

The Tullu Moye pyroclastic deposits are mainly composed of comenditic glass. This tephra group is slightly less evolved (lower SiO₂) compared to the other BBTM tephra deposits. It is characterized by a lower amount of SiO₂ (71.3-73.6 wt%), FeO (1.6-3.5 wt%) and a distinctly higher amount of Al₂O₃ (12.4-15.1 wt%; Fig. 6). These two Tullu Moye deposits (TM-P1 and TM-P2) each also have highly distinct glass compositions, as revealed by their separate clusters in all major element bivariate diagrams (Fig. 6-7). TM-P1 is characterised by a higher TiO₂, Al₂O₃, CaO, K₂O (Fig. 7) and MgO (not plotted) contents relative to TM-P2. TM-P2 is relatively more evolved than TM-P1 and contains higher contents of SiO₂, Na₂O and FeO (Fig. 6-7).

The tephra deposits from Oda, Werdi and Bora show significant compositional heterogeneity in the glass major element composition. The melt compositions span from comenditic to pantelleritic and many fall near the compositional divide on the peralkaline classification diagram (Fig. 6b). Many samples in this population overlap with the highly

evolved (high-SiO₂) end of the pantelleritic rhyolites. The FeO and Al₂O₃ contents can be used to discriminate some of the tephra units in this population. For example, glasses from Od-P1, Od-P2, Od-P3, Od-P4 and Wd-P2 have slightly lower FeO (<5 wt%) and higher Al₂O₃ (>9.1 wt%) contents than the other samples in this group. In contrast, deposits such as Od-P7, Wd-P3 and Wd-P1 have higher FeO (>~6 wt%) and lower Al₂O₃ (<9 wt%) contents. The other tephra units in this population show a wide variation of FeO (3.9-7 wt%) and Al₂O₃ (7.8-11 wt%) contents. The other major element contents like silica and the total alkali contents show less variation (Fig. 6a). One uncorrelated tephra unit exposed at MER150 shows a similar (comenditic) composition to Oda and Werdi deposits (Fig. 6-7). The field, componentry and petrographic data show that this MER150 tephra is likely sourced from a small pumice cone located in the SW part of the complex. In this deposit, there is a strikingly clear chemical variation from comendite to less evolved pantellerites through the stratigraphy.

4.2.2. Trace element composition

To investigate the compositional variability of the BBTM tephra deposits in more detail, trace element glass data were obtained on a selection of samples already analysed by EPMA. The average glass trace element compositions of the analysed tephra layers are presented in Table 3, with the full dataset in Supplementary information (SM-5). The geochemical group revealed by the major element data (section 4.2.1) are also evident in the trace element compositions (Fig. 8). The pantelleritic samples (e.g. Baricha) have systematically higher concentrations of incompatible trace elements (e.g. Zr, Rb, Y, La, Ce) than the comendites (e.g. Tullu Moye). The trace element glass data further highlight

significant compositional variation within the pantellerite population between Baricha and the other tephra deposits (Fig. 8). Baricha glasses have higher Zr (>1500 ppm), Rb (>200 ppm), Y (>150 ppm), La (>150 ppm) and Ce (>300 ppm) contents relative to those from Oda, Suke, Meki and Bora. Other trace elements such as Nb, Cs, Pb and other REEs are also more enriched in the Baricha samples. The only analysed trace elements that are depleted in the pantellerites relative to the comendites are Ba and Sr. The Ba and Sr contents indicate, again, that the oldest Tullu Moya unit (TM-P1; Ba: 550 ± 50 ppm and Sr: 50 ± 10 ppm) is compositionally distinct from the youngest unit (TM-P2; Ba: 400 ± 50 ppm and Sr: 10 ± 3 ppm) (Fig. 8).

Unlike the major element compositions, Aluto tephra trace element compositions (McNamara et al. 2018) show distinct differences with those of Baricha, Meki and Suke samples, especially in Ba and REE content (Fig. 8).

4.3. Eruptive Volume and Magnitude

The tephra fall volume for 12 major eruptions is estimated by manually constructing isopach maps (Fig. 9). Unfortunately, the Suke, Meki and 13 post-caldera deposits are not sufficiently exposed over multiple locations to provide an estimate on volume. Two deposits (Ba-P4 and Ba-P5) were identified in multiple locations covering a large enough area so that more than two isopach contour lines could be constructed (Fig. 9a-b). We calculated the minimum bulk deposit volume for these two deposits using the 1-segment exponential thickness decay model of Pyle (1989). The limited exposure does not allow multiple segments to be identified on a thickness-area trend (Bonadonna et al. 1998) and thus other methods to estimate deposit volume, typically requiring additional constraints (e.g.

Bonadonna & Houghton 2005), are not suitable in this case. For the 10 remaining deposits identified in multiple locations (Ba-P2, Ba-P3, Ba-P6, Ba-P7, Od-P4, Od-P5, Wd-P2, Wd-P1 and TM-P2), only one or two contour lines can be inferred, and for these we use the Legros (2000) one-isopach method to estimate their minimum bulk volume. The bulk volume estimation of these deposits falls in the range 0.007 km³ to 1.1 km³. The componentry data of these deposits indicates the lithic content is very low (<10% in the fraction below 4 mm) compared to the juvenile proportion. Therefore, we only considered the pumice when converting the bulk deposit volume to a dense rock equivalent (DRE) volume, by assuming 2300 kg/m³ rhyolite melt density (Fierstein & Hildreth 1992) and 470 kg/m³ average bulk density as measured on BBTM deposits. The DRE volume of major BBTM eruptions is thus estimated between 0.001 km³ to 0.22 km³. These estimates were then used to calculate minimum magnitude of these eruptions using the following relationship: Magnitude = log₁₀ [erupted mass, kg] - 7 (Pyle 2015). Based on the preserved deposits, most magnitude estimates range from 3.9 to 4.7 for eruptions from Werdi, Oda, Bora and Baricha (see supplementary material SM-6). The youngest Tullu Moye eruption however has a lower minimum magnitude of 2.5. The three Baricha eruptions that are most widespread, up to 20 km west of the edifice (Ba-P4, Ba-P5 and Ba-P7) have a minimum estimated magnitude of 4.6 to 4.7.

5. Discussion

5.1. Tephrostratigraphy and Correlation

Eruptive deposits from the BBTM volcanic complex overlay a series of older volcanic rocks (Fig. 2b). The base of the BBTM sequence observed in the field (this work) and in shallow

wells (Ayele et al. 2002) comprises welded ignimbrite and lavas of different composition (rhyolite, trachyte and basalt). This series blankets the rift floor and in different parts of the MER is known as the Nazret unit (Kazmin & Berhe 1978). An obsidian flow and ignimbrite of this series collected near Tullu Moya volcano yields a late Pleistocene age of 1.58 ± 0.2 Ma (WoldeGabriel et al. 1990) which is coeval to the development of the Wonji Fault Belt (WFB) along the MER axis (1.6 Ma; Ebinger & Casey 2001). This older unit is related to pre-BBTM volcanism and may be associated with the start of tectono-magmatic focusing along the axial zone of the MER.

The oldest deposit recognised in our work, the Suke deposit, is primarily composed of large boulders and blocks of poorly-vesiculated pumice and obsidian lithics at the type section (MER253; Fig. 2). A few kilometres SE from the type section, this unit becomes finer-grained with a more prominent ashy matrix. We interpret the Suke deposit as an unwelded ignimbrite unit, with its very coarse facies a “pumice and lithic lag breccia”, commonly interpreted to represent the onset of caldera collapse (e.g. Druitt & Sparks 1982; Jordan et al. 2018; Seggiaro et al. 2019). The dense and coarse blocks, possibly partially related to vent erosion or widening, thus segregated from the PDCs which then carried relatively finer material further from the source (Druitt & Sparks 1982; Druitt 1985; Walker 1985). The juvenile volcanic products have no datable material (i.e. sanidine) and thus the absolute age of the Suke caldera-forming event remains unconstrained.

The Meki deposit directly overlays deposits of the Suke caldera-forming eruption. A faint weathered horizon at the top of the Suke deposits indicates a hiatus and testifies that the two units represent different eruptions. The glass compositions further support this interpretation, with a clear difference in Al_2O_3 and FeO contents between the two deposits

(Fig. 6b, 7a-d). The Meki deposit is a very thick fall (>20 m; cumulative of at least two horizons) and PDC (>13 m) deposit at 20-25 km distance from the centre of BBTM volcanic complex. At these medial locations (20-25 km from the vent) three main distinct horizons are observed in the Meki deposit. These horizons are massive tephra fall at the base and top, separated by alternating tephra fall and poorly sorted PDC deposits. Across this sequence, the deposits are characteristically lithic-free, which can be partially used as a diagnostic feature to identify them in the field. The brown surficial staining on the pumice deposits at ca. 1660 m asl. and the deposits age (107.7 ± 8.8 ka) suggest that the Meki eruption possibly pre-dates with the lake-level high stand of the oldest megalake phase that covered most of the Central MER (Benvenuti et al. 2002), including the western portion of the BBTM volcanic system.

Despite the lithic-free nature of the deposits, and relative limited exposure preventing volume estimates, the large thickness of the deposits and distance to the source, leads us to suggest that the Meki eruption may have led to another caldera collapse. Other volcanic complexes in the Central MER had caldera-forming eruptions at 180 ± 30 ka (Corbetti), 306 ± 12 to 316 ± 19 ka (Aluto) and 282 ± 110 ka (Gedemsa; Hutchison et al. 2016a, b). The 107.7 ± 8.8 ka Meki eruption may thus be the youngest caldera-forming event in the central sector of the MER, and is also notably younger than the hypothesised ignimbrite flare-up window (320 to 170 ka) proposed by Hutchison et al. (2016b). Additional age constraints on Central MER caldera-forming eruptions, such as the Suke ignimbrite, are required to test the flare-up hypothesis. Due to extensive post-caldera activity, the dimensions and geometry of the inferred caldera associated with the large Suke and Meki eruptions are difficult to trace. However, there are some possible remnants visible on the hill-shade map on Figure 2a and

noted by Korme et al. (2004) as “Tullu caldera” that requires further study to establish any association with the large eruptions documented here.

As reported in several case studies, caldera-forming eruptions may experience a transition from a single-vent phase to a subsidence-related multiple vent phase along a ring structure in the post-caldera sequence of events (e.g. Druitt & Sparks 1984; Lipman 1984; Heiken & McCoy 1984; Hildreth & Mahood 1986). The BBTM experienced both effusive and explosive volcanism during its post-caldera stage, forming both lavas and pyroclastic deposits (Di Paola 1972; Fontijn et al. 2018; this work). The widespread tephra deposits were identified to originate from the Baricha, Bora, Oda, Werdi and Tullu Moye edifices (section 4.1). In proximal sequences, we find deposit characteristics, such as the presence of ballistics, expanded clasts, coarse-grained pumice and lithic breccias. The stratigraphic relationship between the caldera-forming and post-caldera deposits can be observed in some sections, with palaeosols developed on top of the former, indicating a hiatus. One post-caldera eruption in the Baricha sequence (Ba-P5) was dated at 87 ± 16 ka and is underlain by at least 4 more post-caldera eruptions. The pause in volcanic activity following the youngest caldera-forming eruption (Meki) is thus at most on the order of thousands to a few tens of thousands of years at BBTM. This is distinctly shorter than the inferred 250 ky hiatus identified by Hutchison et al. (2016a) at Aluto following the caldera-forming event.

The Meki deposit is entirely lithic-free, whereas the post-caldera deposits contain some lithics. This may be related to a restructuring of the plumbing system caused by the caldera collapse (e.g. Hildreth & Mahood 1986), competence variation of rocks at fragmentation depth (Aravena 2017) and/or possible presence of a lithic-dominated deposit horizon other than the Meki one at depth. The lithic components in the post-caldera deposits are mainly

composed of green ignimbrite, rhyolite, basalt and obsidian lava. The subsurface geology of BBTM, observed in the shallow drill cuttings (Ayele et al. 2002; Fig. 2b) shows an ignimbrite and lava series similar to these lithic components. This may indicate that the lithic components in the deposits are mainly sourced from vent erosion at a relatively deep level (5-170 m).

The glass composition of Suke, Meki, Baricha and some Bora tephras are pantelleritic and show a lot of similarities (e.g. 70-78 wt% SiO₂), even in the trace element contents. This creates a practical complication for the correlation of the deposits based on glass chemistry alone. This chemical homogeneity is commonly found in highly evolved tephra deposits (e.g. Toba: Smith et al. 2011; Ciomadul: Harangi et al. 2020; Aeolian Islands: Albert et al. 2017; Corbetti: Fontijn et al. 2018; Martin-Jones et al. 2017). Other characteristics, e.g. componentry, are thus required to help correlate the units. Notably, the Baricha tephra deposits are the only units that do not contain any lithics of hydrothermally altered reddish lava, in stark contrast to the Bora units. In addition, the absence of lithics in Meki is diagnostic and allows it to be distinguished from other BBTM deposits.

The pumice cone deposits that outcrop around the major centres likely represent relatively small-scale eruptions. They are characterised by significant deposit thinning over short spatial distance and fall-PDC successions consistent with alternating sustained columns and plume collapses (Clarke et al. 2019).

The glass major element chemistry of the BBTM deposits overlaps with that of the Aluto and Corbetti deposits. However, the trace element data, especially Ba and some REEs, differ and can be used to discriminate BBTM from Aluto compositions. The generally higher

incompatible trace element concentrations of Meki indicate that the melt was more evolved than at Aluto.

5.2. BBTM Eruptive Frequency

Based on the established tephrostratigraphic framework, we can constrain the overall eruptive frequency of BBTM. BBTM experienced at least two caldera-forming eruptions, the most recent one (Meki) at 107.7 ± 8.8 ka. After this eruption, post-caldera volcanic centres such as Baricha, Bora, Oda, Werdi and Tullu Moya together erupted explosively at least 25 times within the last 100-116 ky and that left pyroclastic deposits that can be traced in multiple locations. In addition, more than 7 non-correlated units are identified, each likely representing a single eruption. Therefore, on average at least one explosive eruption occurred per 3000-4000 years in the BBTM volcanic system. Of these post-caldera explosive eruptions, three are attributed to Bora, eight to Oda, three to Werdi and two to Tullu Moya. Additionally, Baricha volcano was the source of at least nine eruptions. For two Baricha eruptions, we were able to constrain an absolute age: the Ba-P5 eruption occurred at 87 ± 16 ka and the Ba-P9 eruption (the youngest that is preserved in the record) occurred at 1190 ± 36 cal yr BP. This shows that Baricha had at least 5 eruptions within the first ca. 20,000 years after the Meki eruption and then at least 4 more eruptions since ca. 87 ka. Since younger and/or larger eruption products are expected to be preferentially preserved relative to older and/or smaller deposits (Brown et al. 2014), the geological records are may be biased. The chronological (and magnitude) constraints on our present stratigraphic framework are unfortunately too incomplete to allow inferring any changes in eruption frequency or rate through time at BBTM. Our magnitude (Section 4.3) estimations suggest

776 that the BBTM volcanic complex has experienced at least 11 post-caldera explosive
777 eruptions with a magnitude of 4 or above (Section 4.3) within the last ca. 100,000 years.
778 Note that our evaluations of eruption frequency and magnitude do not take into account
779 the effusive eruptive products and are also based on minimum frequency and eruptive
780 volume estimations that are certainly influenced by deposit preservation and/or deposit
781 thinning behaviour (e.g. Bonadonna & Houghton 2005). Regardless, compared to other
782 volcanic complexes in the region, such as Aluto and Corbetti, BBTM seems less frequently
783 active in terms of explosive eruptions. However, BBTM may be more frequently active, and
784 characterised by higher-magnitude post-caldera eruptions, compared to the volcanic
785 systems located further north (e.g. Boset-Bericha and Fentale), which experienced several
786 effusive and a more limited number of explosive eruptions in their recent past (e.g. Fontijn
787 et al. 2018; Siegburg et al. 2018). The combined terrestrial and lacustrine records of Corbetti
788 tephra indicate an explosive eruption every ca. 700-1000 years (Fontijn et al. 2018; Martin-
789 Jones et al. 2017). The lacustrine record provides detailed constraints on the Holocene
790 eruptive history of the volcano by supplementing the terrestrial records (Martin-Jones et al.
791 2017). The Wendo Koshe Younger Pumice (WKYP) has an estimated minimum volume of 1.3
792 km³ (Rapprich et al. 2016; Fontijn et al. 2018), or a magnitude of 4.8 using the same
793 approach as above. In the post-caldera phase, at least during the Holocene, Aluto had an
794 average of 3 eruptions per 1000 years (Martin-Jones et al. 2017; Fontijn et al. 2018;
795 McNamara et al. 2018). Considering the rapid thinning trend of the relatively well-
796 documented Qup deposit, Fontijn et al. (2018) roughly estimated a magnitude of 3 for this
797 pumice cone eruption. There is very little information regarding eruption magnitude for
798 other volcanoes in the MER to make a quantitative comparison. However, from the

available information (WKYP: $M=4.8$ and Qup: $M\sim 3$) we conclude that BBTM has eruptions of at least comparable magnitude than Corbetti and Aluto in their post-caldera phase.

5.3. Hazard Implications

The tephrostratigraphic record of BBTM provides evidence for at least two major caldera-forming events and 25 moderate-scale explosive eruptions. The spatial distribution of the deposits of caldera-forming eruptions is poorly constrained because of the abundant post-caldera deposits that conceal them. The second caldera-forming eruption, Meki, has better exposures that document its tephra dispersion. This eruption deposited >20 m tephra fall and >13 m PDCs at medial locations, and >1.1 m tephra fall at distal regions. The established frequency-magnitude information in section 5.1 indicates an explosive eruption occurs from BBTM at least every 3000-4000 yrs. The isopach maps of the well-dispersed post-caldera deposits (Ba-P4 and Ba-P5) indicate dispersion of tephra up to at least 20 km from the volcanic centre, for example in the town of Alem Tena, where deposits are still 1 m thick. These eruptions also accumulated up to 5 m thick deposits in the proximal exposures located within 4 to 5 km of the vent. Oda emplaced clast-supported to matrix-supported PDCs during the penultimate identified eruption (Od-P7). This deposit is identified in a valley that was formed by an intermittent stream that feeds Ziway Lake. Near the base of the Oda edifice, it is 16 m thick and 10 km away it still is 1.5 m thick. In general, from the spatial distribution of the pyroclastic deposits, we can conclude that several BBTM eruptions covered a surface with a radius of at least 25 km.

Within this 25 km radius from any of the main centres, there are numerous urban and rural settlements with highly variable population densities (Fig. 2a). The towns of Alem Tena (10

km from Baricha), Meki (20 km from Bora), Ogolcho (12 km from Oda) and Iteya (11 km from Tullu Moye) are all located within this radius from at least one of the main volcanic vents. Total estimates of around one hundred thousand people are living in these towns and the surrounding rural areas, with many of them highly dependent on agriculture (CSAE 2007). In the towns, with the exception of Iteya, 1 to 20 m thick tephra fall has been deposited during past eruptions. The area is also exposed to tephra fall hazard in the future, and this could cause a major threat to human health and livelihoods, buildings and other infrastructure, economic activities, and ecosystems (e.g. Spence et al. 2005; Wilson et al. 2012). To the West of Meki and Ogolcho, PDC deposits with thicknesses between 1.5 to 13 m also indicate an additional potential volcanic hazard to the BBTM region.

Detailed volcanic hazard assessments can be useful for land-use planning and development of mid-to-long-term risk mitigation strategies. Volcanic hazard maps are often to a large extent based on a volcano's past eruptive history (e.g. Calder et al., 2015). Our current data provide some initial constraints on frequency and magnitude of past eruptions at BBTM, the extent of volcanic deposits inundation and possible related volcanic hazards to the nearby region. Given the high population density and presence of critical infrastructure (e.g. Tullu Moye geothermal facilities) our results may be used as a background for future research in the direction of generating more detailed, potentially probabilistic, volcanic hazard assessment (e.g. Clarke et al. 2020; Tierz et al. 2020) or volcano monitoring activities.

6. Conclusion

A detailed study on the tephrostratigraphic framework of the BBTM tephra deposits has enabled us to reconstruct the past explosive activity of the volcanic complex. Here we

845 present the first detailed stratigraphic record of the explosive eruptions experienced in the
846 BBTM volcanic complex. The field data, glass chemistry (major and trace elements),
847 componentry and petrographic data allow us to identify 27 eruptions that include pumice
848 fall and/or PDC deposits. The first two tephra deposits are associated with two different
849 caldera-forming eruptions: the (1) Suke caldera deposits that are characterized by a lag
850 breccia lithofacies and (2) Meki caldera eruption, represented by a very thick tephra fall and
851 flow succession with an age of 107.7 ± 8.8 (2 σ) ka ($^{40}\text{Ar}/^{39}\text{Ar}$). This new age of the Meki
852 tephra reveals it to be the youngest caldera-forming eruption identified in the Central MER
853 so far. During the post-caldera volcanism, the BBTM underwent at least 25 moderate-major
854 eruptions sourced from Baricha (9), Bora (3), Oda (8), Werdi (3) and Tullu Moye (2) edifices.
855 The melts that formed these deposits are categorized as comenditic (Tullu Moye) and
856 pantelleritic rhyolites based on the major element glass chemistry. The trace element data
857 indicates that the BBTM pantelleritic tephra are more evolved than those of Aluto volcano
858 located to the south of the study area. The componentry of these deposits reveals a
859 significant variation in pumice, lithics and free mineral content within the deposits. The
860 pumice has a very low percentage of phenocrysts (<10%).

861 When we consider the BBTM post-caldera phase only, the recurrence rate of the explosive
862 activity from this extended volcanic system is ≥ 1 eruption per 4000 yrs. This explosive
863 eruption frequency is much lower compared to Aluto and Corbetti, which has been
864 reconstructed from both terrestrial and lacustrine records. The estimated tephra volume for
865 the well exposed units indicates eruption magnitudes pre-dominantly varying from 4 to 5.
866 Only at Tullu Moye deposits of smaller (magnitude 2.5) eruptions were identified in the
867 geological record. For most of the larger eruptions, tephra was dispersed up to 20 km from

the volcanic centre suggesting that more than hundred thousand people could be affected by future eruptions of similar magnitude in this area.

Acknowledgements

AT is supported by the F.R.S.-FNRS Aspirant doctoral fund. Several samples and an extensive glass chemistry dataset were collected under the NERC-funded RiftVolc Large Grant (NE/L013649/1) by KF along with others. We would like to thank Tamsin Mather and David Pyle for giving the permission to access the dataset and samples from the RiftVolc project. KF further acknowledges support from F.R.S.-FNRS MIS grant F.4515.20. The iCRAG LA-ICP-MS facility at Trinity College Dublin is supported by SFI award 13/RC/2092. Field work and sample export was kindly permitted by authorities of the Oromia region and Ministry of Mines and Petroleum of Ethiopia, respectively. Professional logistical support was provided by Ethioder Pvt Ltd Co and their drivers. Mathieu Boudin (KIK-IRPA, Institut Royal du Patrimoine Artistique) handled the radiocarbon dating. We thank Thomas Gernon and one anonymous reviewer for detailed and constructive comments which improved the paper.

Reference

Agostini, A., Bonini, M., Corti, G., Sani, F. and Mazzarini, F., 2011. Fault architecture in the Main Ethiopian Rift and comparison with experimental models: implications for rift evolution and Nubia–Somalia kinematics. *Earth and Planetary Science Letters*, 301(3-4): 479-492.

889 Albino, F. and Biggs, J., 2021. Magmatic Processes in the East African Rift System: Insights
 890 From a 2015–2020 Sentinel-1 InSAR Survey. *Geochemistry, Geophysics, Geosystems*,
 891 22(3): e2020GC009488.

892 Albert, P. G., Tomlinson, E. L., Smith, V. C., Di Traglia, F., Pistolesi, M., Morris, A., Donato, P.,
 893 De Rosa, R., Sulpizio, R., Keller, J. and Rosi, M., 2017. Glass geochemistry of pyroclastic
 894 deposits from the Aeolian Islands in the last 50 ka: a proximal database for
 895 tephrochronology. *Journal of Volcanology and Geothermal Research*, 336: 81-107.

896 Aravena, A., 2017. Stability of volcanic conduits: Critical mechanical parameters. *Il nuovo*
 897 *cimento C*, 40(2): 1-9.

898 Aspinall, W. P., Auker, M., Hincks, T., Mahony, S., Nadim, F., Pooley, J., Sparks, R.S.J. and
 899 Syre, E., 2011. Volcano hazard and exposure in GFDRR priority countries and risk
 900 mitigation measures. Volcano Risk Study 0100806-00-1-R. Global Facility for disaster
 901 Reduction and Recovery, Washington, D.C.

902 Ayele, A., Teklemariam, M. and Kebede, S., 2002. Geothermal exploration in the Abaya and
 903 Tulu Moye-Gedemsa prospects, Main Ethiopian Rift. Geological Survey of Ethiopia,
 904 Addis Ababa, 79 pp.

905 Balestrieri, M. L., Bonini, M., Corti, G., Sani, F. and Philippon, M., 2016. A refinement of the
 906 chronology of rift-related faulting in the Broadly Rifted Zone, southern Ethiopia,
 907 through apatite fission-track analysis. *Tectonophysics*, 671: 42-55.

908 Bastow, I. D., Keir, D. and Daly, E., 2011. The Ethiopia Afar Geoscientific Lithospheric
 909 Experiment (EAGLE): Probing the transition from continental rifting to incipient
 910 seafloor spreading. *Volcanism and evolution of the African lithosphere*, 478: 1-26.

911 Benvenuti, M., Carnicelli, S., Belluomini, G., Dainelli, N., Di Grazia, S., Ferrari, G. A., Lasio, C.,
912 Sagri, M., Ventra, D., Atnafu, B. and Kebede, S., 2002. The Ziway–Shala lake basin
913 (main Ethiopian rift, Ethiopia): a revision of basin evolution with special reference to
914 the Late Quaternary. *Journal of African Earth Sciences*, 35(2): 247-269.

915 Benvenuti, M., Bonini, M., Tassi, F., Corti, G., Sani, F., Agostini, A., Manetti, P and Vaselli, O.,
916 2013. Holocene lacustrine fluctuations and deep CO₂ degassing in the northeastern
917 Lake Langano Basin (Main Ethiopian Rift). *Journal of African Earth Sciences*, 77: 1-10.

918 Biggs, J., Bastow, I. D., Keir, D. and Lewi, E., 2011. Pulses of deformation reveal frequently
919 recurring shallow magmatic activity beneath the Main Ethiopian Rift. *Geochemistry,*
920 *Geophysics, Geosystems*, 12(9).

921 Bizouard, H. and Di Paola, G. M., 1978. Mineralogy of the Tullu Moje active volcanic area
922 (Arussi: Ethiopian Rift valley). In *Petrology and Geochemistry of Continental Rifts* (pp.
923 87-100). Springer, Dordrecht.

924 Bonadonna, C., Ernst, G. G. J. and Sparks, R. S. J., 1998. Thickness variations and volume
925 estimates of tephra fall deposits: the importance of particle Reynolds number. *Journal*
926 *of Volcanology and Geothermal Research*, 81(3-4): 173-187.

927 Bonadonna, C. and Houghton, B. F., 2005. Total grain-size distribution and volume of tephra-
928 fall deposits. *Bulletin of Volcanology*. 67(5): 441-456.

929 Bronk Ramsey, C., 2009. Bayesian analysis of radiocarbon dates. *Radiocarbon* 51, 337e360.

930 Brown, S. K., Crosweller, H. S., Sparks, R. S. J., Cottrell, E., Deligne, N. I., Guerrero, N. O.,
931 Hobbs, L., Kiyosugi, K., Loughlin, S.C., Siebert, L. and Takarada, S., 2014.
932 Characterisation of the Quaternary eruption record: analysis of the Large Magnitude

933 Explosive Volcanic Eruptions (LaMEVE) database. *Journal of Applied Volcanology*, 3(1):
934 1-22.

935 Cas, R., Porritt, L., Pittari, A. and Hayman, P., 2008. A new approach to kimberlite facies
936 terminology using a revised general approach to the nomenclature of all volcanic rocks
937 and deposits: descriptive to genetic. *Journal of Volcanology and Geothermal Research*,
938 174(1-3): 226-240.

939 Calder, E.S., Wagner, K. and Ogburn, S.E., 2015. Volcanic hazard maps. In: Loughlin, S.C.,
940 Sparks, R.S.J., Brown, S.K., Jenkins, S.F., Vye-Brown, C. (eds). *Global volcanic hazards*
941 *and risk*, Cambridge. Cambridge University Press, 335-342.

942 Central Statistical Agency of Ethiopia (CSAE), 2007. The 2007 Population and Housing Census
943 of Ethiopia: Statistical Report for Oromiya Region; Part I: Population Size and
944 Characteristics. Report, Addis Ababa, Ethiopia.

945 Clarke, B., Calder, E. S., Dessalegn, F., Fontijn, K., Cortés, J. A., Naylor, M., Butler, I.,
946 Hutchison, W. and Yirgu, G., 2019. Fluidal pyroclasts reveal the intensity of peralkaline
947 rhyolite pumice cone eruptions. *Nature communications*, 10(1): 1-10.

948 Clarke, B. A., Tierz, P., Calder, E. S. and Yirgu, G., 2020. Probabilistic volcanic hazard
949 assessment for pyroclastic density currents from pumice cone eruptions at Aluto
950 volcano, Ethiopia. *Frontiers in Earth Science*, 348.

951 Daly, E., Keir, D., Ebinger, C. J., Stuart, G. W., Bastow, I. D. and Ayele, A., 2008. Crustal
952 tomographic imaging of a transitional continental rift: the Ethiopian rift. *Geophysical*
953 *Journal International*, 172(3): 1033-1048.

954 Di Paola, G. M., 1972. The Ethiopian Rift Valley (between 7 00' and 8 40' lat. north). Bulletin
955 Volcanologique, 36(4): 517-560.

956 Donovan, A. and Oppenheimer, C., 2012. Governing the lithosphere: insights from
957 Eyjafjallajökull concerning the role of scientists in supporting decision-making on
958 active volcanoes. Journal of Geophysical Research: Solid Earth, 117(B3).

959 Druitt, T. H., 1985. Vent evolution and lag breccia formation during the Cape Riva eruption
960 of Santorini, Greece. The Journal of Geology, 93(4): 439-454.

961 Druitt, T. H. and Sparks, R. S. J., 1982. A proximal ignimbrite breccia facies on Santorini,
962 Greece. Journal of Volcanology and Geothermal Research, 13(1-2): 147-171.

963 Druitt, T. H. and Sparks, R. S. J., 1984. On the formation of calderas during ignimbrite
964 eruptions. Nature, 310(5979): 679-681.

965 Ebinger, C., 2005. Continental break-up: the East African perspective. Astronomy &
966 Geophysics, 46(2): 2-16.

967 Ebinger, C. J., Yemane, T., Harding, D. J., Tesfaye, S., Kelley, S. and Rex, D. C., 2000. Rift
968 deflection, migration, and propagation: Linkage of the Ethiopian and Eastern rifts,
969 Africa. Geological Society of America Bulletin, 112(2): 163-176.

970 Ebinger, C. J. and Casey, M., 2001. Continental breakup in magmatic provinces: An Ethiopian
971 example. Geology, 29(6): 527-530.

972 Electroconsult (ELC), 1978. Geothermal reconnaissance study of selected sites of the
973 Ethiopian rift system. Geological report, Milano, Italy.

974 Fierstein, J. and Hildreth, W., 1992. The plinian eruptions of 1912 at Novarupta, Katmai
975 national park, Alaska. Bulletin of Volcanology, 54(8): 646-684.

976 Fontijn, K., McNamara, K., Tadesse, A. Z., Pyle, D. M., Dessalegn, F., Hutchison, W., Mather,
977 T.A. and Yirgu, G., 2018. Contrasting styles of post-caldera volcanism along the Main
978 Ethiopian Rift: Implications for contemporary volcanic hazards. *Journal of Volcanology*
979 and *Geothermal Research*, 356: 90-113.

980 Froggatt, P. C., 1983. Toward a comprehensive Upper Quaternary tephra and ignimbrite
981 stratigraphy in New Zealand using electron microprobe analysis of glass shards.
982 *Quaternary research*, 19(2): 188-200.

983 Gouin, P., 1979. Earthquake history of Ethiopia and the Horn of Africa. IDRC, Ottawa, ON,
984 CA.

985 Greenfield, T., Keir, D., Kendall, J. M. and Ayele, A., 2019a. Low-frequency earthquakes
986 beneath Tullu Moya volcano, Ethiopia, reveal fluid pulses from shallow magma
987 chamber. *Earth and Planetary Science Letters*, 526: 115782.

988 Greenfield, T., Keir, D., Kendall, J. M. and Ayele, A., 2019b. Seismicity of the Bora-Tullu Moya
989 Volcanic Field, 2016–2017. *Geochemistry, Geophysics, Geosystems*, 20(2): 548-570.

990 Harangi, S., Molnár, K., Schmitt, A. K., Dunkl, I., Seghedi, I., Novothny, Á., Molnár, M., Kiss,
991 B., Ntaflos, T., Mason, P.R. and Lukács, R., 2020. Fingerprinting the Late Pleistocene
992 tephras of Ciomadul volcano, eastern–central Europe. *Journal of Quaternary Science*,
993 35(1-2): 232-244.

994 Heiken, G. and McCoy Jr, F., 1984. Caldera development during the Minoan eruption, Thira,
995 Cyclades, Greece. *Journal of Geophysical Research: Solid Earth*, 89(B10): 8441-8462.

996 Hildreth, W. and Mahood, G. A., 1986. Ring-fracture eruption of the Bishop Tuff. *Geological*
997 *Society of America Bulletin*, 97(4): 396-403.

998 Houghton, B. F. and Wilson, C. J. N., 1989. A vesicularity index for pyroclastic deposits.
999 Bulletin of volcanology, 51(6): 451-462.

1000 Hutchison, W., Fusillo, R., Pyle, D. M., Mather, T. A., Blundy, J. D., Biggs, J., Yirgu, G., Cohen,
1001 B.E., Brooker, R.A., Barfod, D.N. and Calvert, A. T., 2016a. A pulse of mid-Pleistocene
1002 rift volcanism in Ethiopia at the dawn of modern humans. Nature Communications,
1003 7(1): 1-12.

1004 Hutchison, W., Pyle, D. M., Mather, T. A., Yirgu, G., Biggs, J., Cohen, B. E., Barfod, D.N. and
1005 Lewi, E., 2016b. The eruptive history and magmatic evolution of Aluto volcano: new
1006 insights into silicic peralkaline volcanism in the Ethiopian rift. Journal of Volcanology
1007 and Geothermal Research, 328: 9-33.

1008 Hutchison, W., Biggs, J., Mather, T. A., Pyle, D. M., Lewi, E., Yirgu, G., Caliro, S., Chiodini, G.,
1009 Clor, L.E. and Fischer, T. P., 2016c. Causes of unrest at silicic calderas in the East
1010 African Rift: New constraints from InSAR and soil-gas chemistry at Aluto volcano,
1011 Ethiopia. Geochemistry, Geophysics, Geosystems, 17(8): 3008-3030.

1012 Jochum, K. P., Stoll, B., Herwig, K., Willbold, M., Hofmann, A. W., Amini, M., Aurburg, S.,
1013 Abouchami, W., Hellebrand E. and Raczek, I., 2006. MPI-DING reference glasses for in
1014 situ microanalysis: New reference values for element concentrations and isotope
1015 ratios. Geochemistry, Geophysics, Geosystems, 7(2).

1016 Jochum, K. P., Weis, U., Stoll, B., Kuzmin, D., Yang, Q., Raczek, I., Jacobe, D.E, Stracke, A.,
1017 Birbaum, K., Frick, D.A. and Günther, D., 2011. Determination of reference values for
1018 NIST SRM 610–617 glasses following ISO guidelines. Geostandards and Geoanalytical
1019 Research, 35(4): 397-429.

1020 Jordan, N. J., Rotolo, S. G., Williams, R., Speranza, F., McIntosh, W. C., Branney, M. J. and
 1021 Scaillet, S., 2018. Explosive eruptive history of Pantelleria, Italy: Repeated caldera
 1022 collapse and ignimbrite emplacement at a peralkaline volcano. *Journal of Volcanology*
 1023 *and Geothermal Research*, 349: 47-73.

1024 Kazmin, V. and Berhe, S. M., 1978. Geology and development of the Nazret area. Northern
 1025 Ethiopian Rift sheet NC37–15, Memoir, 3: 26.

1026 Keir, D., Ebinger, C. J., Stuart, G. W., Daly, E. and Ayele, A., 2006. Strain accommodation by
 1027 magmatism and faulting as rifting proceeds to breakup: Seismicity of the northern
 1028 Ethiopian rift. *Journal of Geophysical Research: Solid Earth*, 111(B5).

1029 Korme, T., Acocella, V. and Abebe, B., 2004. The role of pre-existing structures in the origin,
 1030 propagation and architecture of faults in the Main Ethiopian Rift. *Gondwana Research*,
 1031 7(2): 467-479.

1032 Le Bas, M. J., Maitre, R. L., Streckeisen, A., Zanettin, B. and IUGS Subcommittee on the
 1033 Systematics of Igneous Rocks, 1986. A chemical classification of volcanic rocks based
 1034 on the total alkali-silica diagram. *Journal of petrology*, 27(3): 745-750.

1035 Legros, F., 2000. Minimum volume of a tephra fallout deposit estimated from a single
 1036 isopach. *Journal of Volcanology and Geothermal Research*, 96(1-2): 25-32.

1037 Le Turdu, C., Tiercelin, J. J., Gibert, E., Travi, Y., Lezzar, K. E., Richert, J. P., Massault, M.,
 1038 Gesse, F., Bonnefille, R., Decobert, M. and Gensous, B., 1999. The Ziway–Shala lake
 1039 basin system, Main Ethiopian Rift: influence of volcanism, tectonics, and climatic
 1040 forcing on basin formation and sedimentation. *Palaeogeography, Palaeoclimatology,*
 1041 *Palaeoecology*, 150(3-4): 135-177.

1042 Lipman, P. W., 1984. The roots of ash flow calderas in western North America: windows into
 1043 the tops of granitic batholiths. *Journal of Geophysical Research: Solid Earth*, 89(B10):
 1044 8801-8841.

1045 Loughlin, S. C., Sparks, R. S. J., Sparks, S., Brown, S. K., Jenkins, S. F. and Vye-Brown, C., 2015.
 1046 *Global volcanic hazards and risk*. Cambridge University Press.

1047 Lowe, D. J., 2011. Tephrochronology and its application: a review. *Quaternary*
 1048 *Geochronology*, 6(2): 107-153.

1049 Macdonald, R., 1974. Nomenclature and petrochemistry of the peralkaline oversaturated
 1050 extrusive rocks. *Bulletin volcanologique*, 38(2): 498-516.

1051 Mamo, T., 2002. Surface hydrothermal alteration in the Tullu Moye area, Lakes district rift,
 1052 Ethiopia. Geological Survey of Ethiopia, Addis Ababa, 7 pp.

1053 Martin-Jones, C. M., Lane, C. S., Pearce, N. J., Smith, V. C., Lamb, H. F., Schaebitz, F.,
 1054 Viehberg, F., Brown, M.C., Frank, U. and Asrat, A., 2017. Recurrent explosive eruptions
 1055 from a high-risk Main Ethiopian Rift volcano throughout the Holocene. *Geology*,
 1056 45(12): 1127-1130.

1057 McNamara, K., Cashman, K. V., Rust, A. C., Fontijn, K., Chalié, F., Tomlinson, E. L. and Yirgu,
 1058 G., 2018. Using lake sediment cores to improve records of volcanism at Aluto volcano
 1059 in the Main Ethiopian Rift. *Geochemistry, Geophysics, Geosystems*, 19(9): 3164-3188.

1060 Mulugeta, B. D., Fujimitsu, Y., Nishijima, J. and Saibi, H., 2021. Interpretation of gravity data
 1061 to delineate the subsurface structures and reservoir geometry of the Aluto–Langano
 1062 geothermal field, Ethiopia. *Geothermics*, 94: 102093.

- 1063 Niespolo, E. M., Rutte, D., Deino, A. L. and Renne, P. R., 2017. Intercalibration and age of the
1064 Alder Creek sanidine $^{40}\text{Ar}/^{39}\text{Ar}$ standard. *Quaternary Geochronology*, 39: 205-213.
- 1065 Peccerillo, A., Barberio, M. R., Yirgu, G., Ayalew, D., Barbieri and Wu, T. W., 2003.
1066 Relationships between mafic and peralkaline silicic magmatism in continental rift
1067 settings: a petrological, geochemical and isotopic study of the Gedemsa volcano,
1068 central Ethiopian rift. *Journal of Petrology*, 44(11): 2003-2032.
- 1069 Polacci, M., Pioli, L. and Rosi, M., 2003. The Plinian phase of the Campanian Ignimbrite
1070 eruption (Phlegrean Fields, Italy): evidence from density measurements and textural
1071 characterization of pumice. *Bulletin of Volcanology*, 65(6): 418-432.
- 1072 Pyle, D. M., 1989. The thickness, volume and grainsize of tephra fall deposits. *Bulletin of*
1073 *Volcanology*, 51(1): 1-15.
- 1074 Pyle, D. M., 2015. Sizes of volcanic eruptions. In *The encyclopedia of volcanoes* (pp. 257-
1075 264). Academic Press.
- 1076 Rapprich, V., Žáček, V., Verner, K., Erban, V., Goslar, T., Bekele, Y., Legesa, F., Hroch, T. and
1077 Hejtmánková, P., 2016. Wendo Koshe Pumice: The latest Holocene silicic explosive
1078 eruption product of the Corbetti volcanic system (southern Ethiopia). *Journal of*
1079 *Volcanology and Geothermal Research*, 310: 159-171.
- 1080 Reimer, P. J., Austin, W. E., Bard, E., Bayliss, A., Blackwell, P. G., Ramsey, C. B., Butzin, M.,
1081 Cheng, H., Edwards, R.L., Friedrich, M. and Talamo, S., 2020. The IntCal20 Northern
1082 Hemisphere radiocarbon age calibration curve (0–55 cal kBP). *Radiocarbon*, 62(4):
1083 725-757.

1084 Renne, P. R., Balco, G., Ludwig, K. R., Mundil, R. and Min, K., 2011. Response to the
 1085 comment by WH Schwarz et al. on “Joint determination of 40K decay constants and
 1086 $^{40}\text{Ar}^*/^{40}\text{K}$ for the Fish Canyon sanidine standard, and improved accuracy for
 1087 $^{40}\text{Ar}/^{39}\text{Ar}$ geochronology” by PR Renne et al.(2010). *Geochimica et Cosmochimica*
 1088 *Acta*, 75(17): 5097-5100.

1089 Roduit, N., 2019. Image analysis toolbox for measuring and quantifying components of high-
 1090 definition images, JMicroVision: Version 1.3.1. <https://jmicrovision.github.io> (accessed
 1091 10 August 2020).

1092 Rooney, T., Furman, T., Bastow, I., Ayalew, D. and Yirgu, G., 2007. Lithospheric modification
 1093 during crustal extension in the Main Ethiopian Rift. *Journal of Geophysical Research:*
 1094 *Solid Earth*, 112(B10).

1095 Schneider, C.A., Rasband, W.S. and Eliceiri, K. W., 2012. NIH Image to ImageJ: 25 years of
 1096 image analysis. *Nature methods*, 9(7): 671-675.

1097 Seggiaro, R. E., Guzmán, S. R. and Martí, J., 2019. Dynamics of caldera collapse during the
 1098 Coranzulí eruption (6.6 Ma)(Central Andes, Argentina). *Journal of Volcanology and*
 1099 *Geothermal Research*, 374: 1-12.

1100 Siegburg, M., Gernon, T. M., Bull, J. M., Keir, D., Barfod, D. N., Taylor, R. N., Abebe, B. and
 1101 Ayele, A., 2018. Geological evolution of the Boset-Bericha volcanic complex, Main
 1102 Ethiopian Rift: $^{40}\text{Ar}/^{39}\text{Ar}$ evidence for episodic Pleistocene to Holocene volcanism.
 1103 *Journal of Volcanology and Geothermal Research*, 351: 115-133.

1104 Smith, V. C., Pearce, N. J., Matthews, N. E., Westgate, J. A., Petraglia, M. D., Haslam, M.,
 1105 Lane, C.S., Korisettar, R. and Pal, J. N., 2011. Geochemical fingerprinting of the

1106 widespread Toba tephra using biotite compositions. *Quaternary International*, 246(1-
1107 2): 97-104.

1108 Spence, R. J. S., Kelman, I., Baxter, P. J., Zuccaro, G. and Petrazzuoli, S., 2005. Residential
1109 building and occupant vulnerability to tephra fall. *Natural Hazards and Earth System*
1110 *Sciences*, 5(4): 477-494.

1111 Teklemariam, M., Battaglia, S., Gianelli, G. and Ruggieri, G., 1996. Hydrothermal alteration in
1112 the Aluto-Langano geothermal field, Ethiopia. *Geothermics*, 25(6): 679-702.

1113 Tierz, P., Clarke, B., Calder, E. S., Dessalegn, F., Lewi, E., Yirgu, G., Fontijn, K., Crummy, J.M.,
1114 Bekele, Y. and Loughlin, S. C., 2020. Event trees and epistemic uncertainty in long-term
1115 volcanic hazard assessment of rift volcanoes: The example of Aluto (Central Ethiopia).
1116 *Geochemistry, Geophysics, Geosystems*, 21(10).

1117 United Nations Development Programme (UNDP), 1973. *Geology, geochemistry and*
1118 *hydrology of hot springs of the East African Rift system within Ethiopia*. In
1119 *Investigation of geothermal resources for power development (Tech. Rep. DP/SF/UN*
1120 *116, 275 pp.)*. New York, NY: United Nations.

1121 Varet, J. and Birba, E. Tullu Moye Geothermal Project (Oromia, Ethiopia). In *proceedings, 7th*
1122 *African Rift Geothermal Conference, Kigali, Rwanda 31st October – 2nd November*
1123 *2018, 15 pp.*

1124 Walker, G. P., 1985. Origin of coarse lithic breccias near ignimbrite source vents. *Journal of*
1125 *Volcanology and Geothermal Research*, 25(1-2): 157-171.

1126 Wilson, TM, Stewart, C., Sword-Daniels, V., Leonard, GS, Johnston, DM, Cole, JW, Wardman,
 1127 J., Wilson, G. and Barnard, ST., 2012. Volcanic ash impacts on critical infrastructure.
 1128 Physics and Chemistry of the Earth, Parts A / B / C, 45: 5-23.

1129 WoldeGabriel, G., Aronson, J. L. and Walter, R. C., 1990. Geology, geochronology, and rift
 1130 basin development in the central sector of the Main Ethiopia Rift. Geological Society
 1131 of America Bulletin, 102(4): 439-458.

1132

1133 **Figures**

1134 **Figure 1:** Overview map of the MER and its main volcanic and tectonic features. The location
 1135 of the BBTM volcanic system is indicated by a dashed rectangle (for a more detailed view,
 1136 see Fig.2a). Along-rift volcanoes that are considered to be active, with eruptions in the
 1137 Holocene, are indicated by a red triangle. BJVF: Butajira Volcanic Field; DZVF: Debre Zeyt
 1138 Volcanic Field, are mainly basaltic lava and scoria cones located at the MER western margin.
 1139 MER faults after Agostini et al. (2011). Inset shows location of the main map (solid
 1140 rectangle). The Kenyan rift (KR) is connected to the MER by a broadly rifted zone with little
 1141 to no surface expression of magmatism. The MER progresses northwards in the Afar
 1142 Depression forming a triple junction with the Gulf of Aden (GA) and Red Sea (RS) rifts.

1143 **Figure 2:** (A) Map of Bora-Baricha-Tullu Moye volcanic complex showing the distribution of
 1144 different volcanic centres, visited outcrops (the most important of which are labelled with
 1145 three digits referring to their MER outcrops name; SM-3) and shallow drill well sites (see Fig.
 1146 2b; after Ayele et al. 2002). Some outcrops indicated on this figure are the same as those in
 1147 Fontijn et al. (2018). The Werdi vent (spelled also Werdia) is locally also known as Dima. The
 1148 extent of the A-A' profile (Fig. 2b) is indicated by two crosses. (B) West-East (A-A') cross

section showing the sub-surface stratigraphy of BBTM from shallow drill-cores (data from Ayele et al. 2002). The elevation scale on the y axis represents the well stratigraphy; topography is two times vertically exaggerated.

Figure 3: Tephrostratigraphic framework of the BBTM volcanic complex. (A) Baricha, Meki and Suke. (B) Bora, Oda, Werdi and Tullu Moye. Correlations between the different sections are based on stratigraphic position, physical characteristics, petrography and glass chemical composition of the deposits. The relative geographic location in the volcanic system and the scale of the stratigraphic sections are indicated on this figure and can be seen in Fig. 2. The symbols used on geochemical plots of each BBTM unit (Figs. 6-8) are shown for cross-reference.

Figure 4: Field photographs of some of the BBTM pyroclastic deposits. The representative pictures show type sections for Suke (A), Meki (B), Baricha (C), Bora (D), Werdi (E), Oda (F) and Tullu Moye (G) deposits. The symbols are cross referenced to Figure 2 (stratigraphy) and Figures 6-8 (geochemistry).

Figure 5: Componentry and petrography of representative BBTM deposits of (A) Meki, (B) Bora, (C) Werdi, (D) Baricha, (E) Oda and (F) Tullu Moye. For each sample, representative photos illustrating the componentry (left) and petrography (right) are shown, with quantitative results presented on a bar and pie chart respectively. The photos are taken using a stereo zoom and optical petrographic microscope in plane polarised light.

Figure 6: BBTM silicic tephra classification based on major element (wt%) glass composition following (A) Le Bas et al. (1986) and (B) Macdonald (1974). The comparative glass chemistry data for Aluto, Corbetti and Gedemsa volcanoes (dashed lines) are from Fontijn et al. (2018), Martin-Jones et al. (2017) and McNamara et al. (2018).

Figure 7: Bivariate major element (wt%) plots of the BBTM silicic tephra glass compositions. The dashed lines on the diagrams indicate the range of compositions of Aluto, Corbetti and Gedemsa tephra from Fontijn et al. (2018), Martin-Jones et al. (2017) and McNamara et al. (2018). Symbols and colours are the same as in Figure 6.

Figure 8: BBTM tephra trace element (ppm) bivariate and ratio plots. The red dashed line shows the compositional range of Aluto tephra (from McNamara et al. 2018). Symbols and colours are the same as in Figure 6.

Figure 9: Isopach maps (contours in m) for the four major fall deposits from Baricha and Bora, each identified in at least 4 different locations. The minimum (bulk deposit) volume and unit names are indicated on the figures. Volumes are calculated using the Pyle (1989) method for Ba-P4 and Ba-P5, and the Legros (2000) method for Ba-P7 and Bo-P2. Dashed isopach lines are used instead of solid lines where there is great uncertainty in the shape of the contour due to data lack of exposure. The source volcanic centre is indicated by a red triangle and data points by annotated circles.

Tables

Table 1: Compilation of new and existing BBTM age constraints. The $^{40}\text{Ar}/^{39}\text{Ar}$ ages are quoted with 2σ standard error. Radiocarbon dates were calibrated in OxCal v.4.4 (Bronk Ramsey 2009) using the IntCal20 calibration curve (Reimer et al. 2020).

Table 2: Synoptic overview of all BBTM pyroclastic deposits that were identified in multiple outcrops, with a description of their field appearance and laboratory-based observations that have helped establishing correlations between sections (Fig. 3). The major deposits are described in more detail in the text. Mineral abbreviations: alkali feldspar (Kfs), aenigmatite

(Ang), feldspar (Fs), pyroxene (Px), orthopyroxene (Opx), clinopyroxene (Cpx), amphibole (Amp). Th: thickness.

Table 3: Glass major (wt%) and trace (ppm) element composition of BBTM tephra units. Presented data are average compositions (1 sigma standard deviation in brackets) of one representative sample for each unit. The full data set is provided in supplementary material (SM-2 and SM-5). The analysed number of spots per sample for major (n) and trace (N) elements are indicated.

Supplementary Information

Supplementary material 1 (SM-1): SEM-BSE images and EDS spectra on selected points on two BBTM representative samples (MER201H and MER201A).

- **Figure SM-1.1:** (A) BSE image of pumice sample MER201H. (B & C) Glass semi-quantitative EDS spectra for sample spots indicated on the BSE image.
- **Figure SM-1.2:** (A) BSE image of pumice sample MER201A collected from Baricha deposit Ba-P3. (B-D) Semi-quantitative EDS spectra for sample spots indicated on the BSE image of (B) an ilmenite inclusion, (C) a glass rim and (D) an alkali feldspar.

Supplementary material 2 (SM-2): BBTM glass major element dataset analysed by EPMA.

Supplementary material 3 (SM-3): Outcrop locations and names.

Supplementary material 4 (SM-4): BBTM tephra componentry and petrography dataset.

Supplementary material 5 (SM-5): BBTM glass trace element dataset analysed by LA-ICP-MS.

1216 **Supplementary material 6 (SM-6):** Tephra volume and magnitude estimates of major BBTM
1217 explosive eruptions.

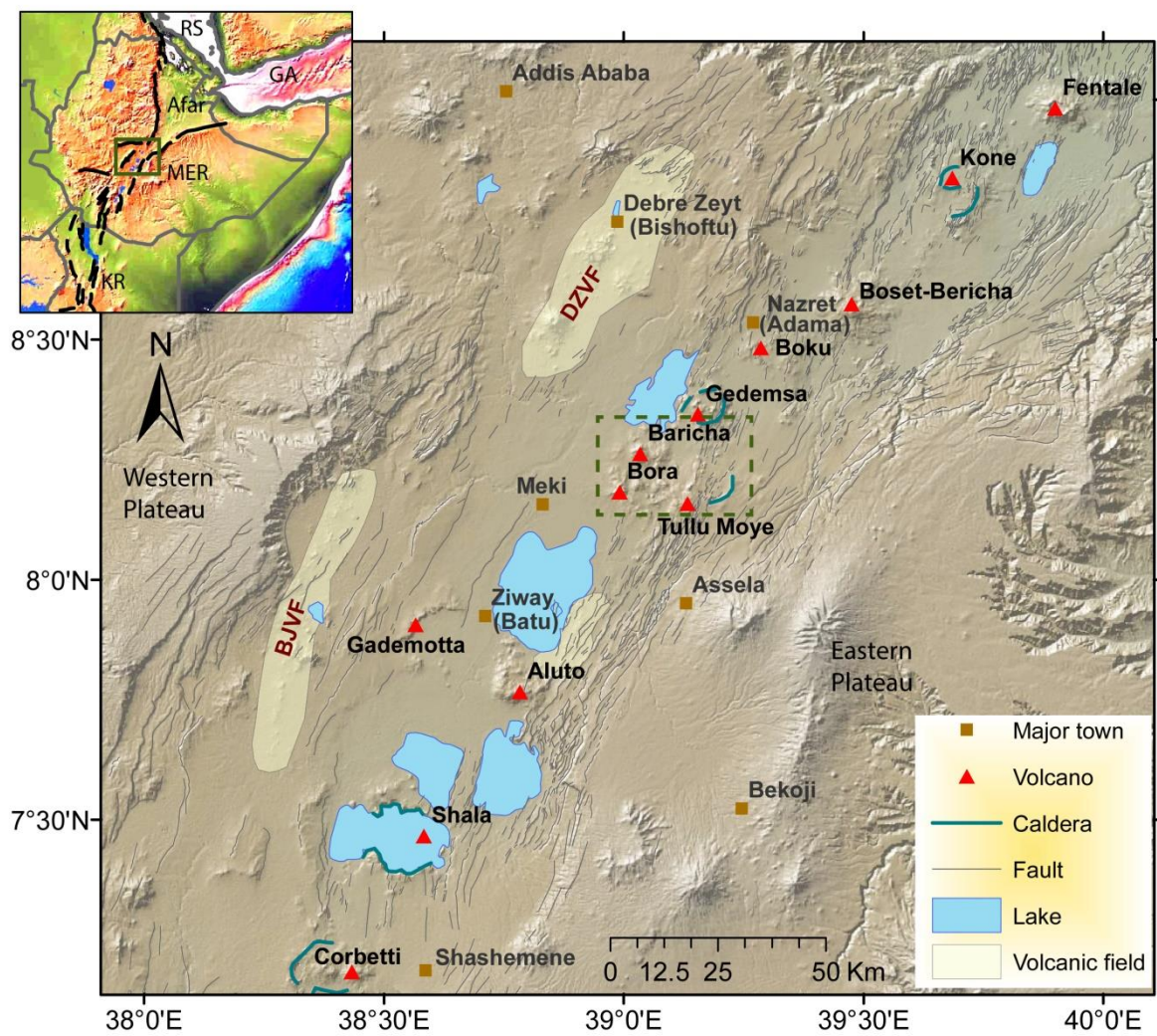


Figure 1

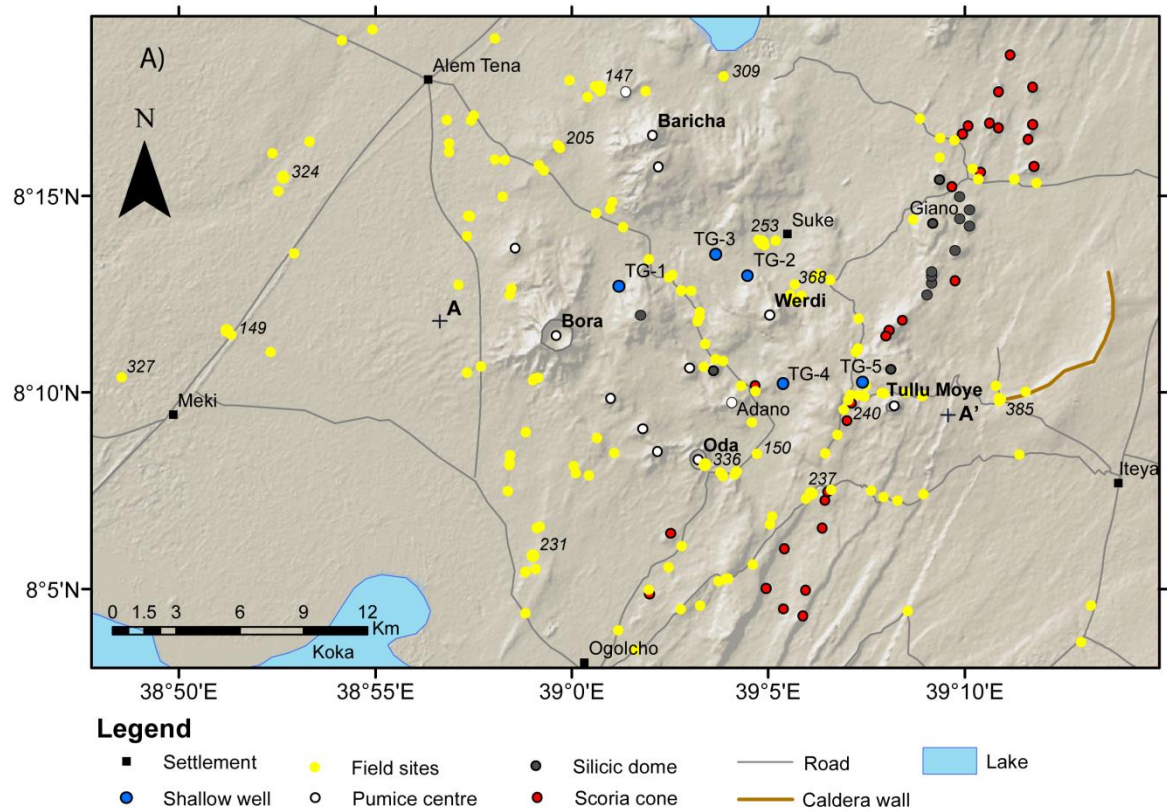


Figure 2a

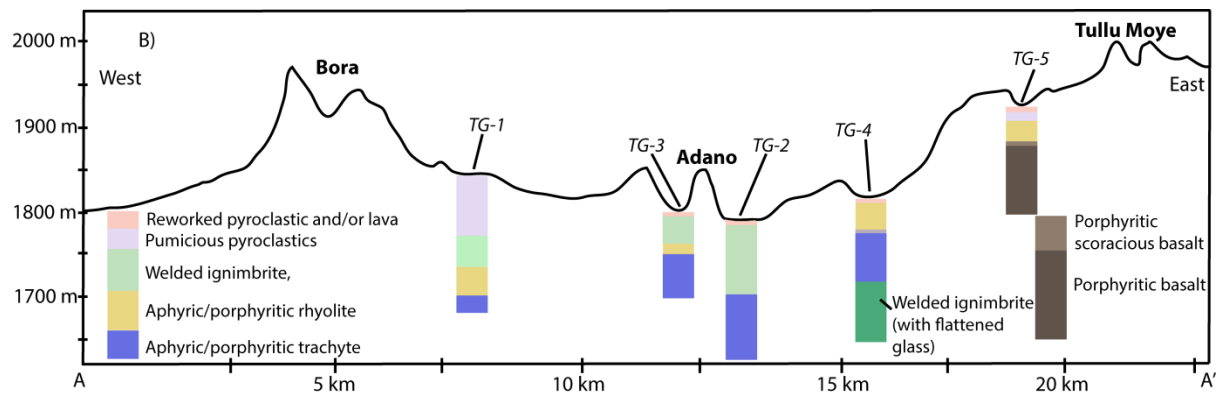


Figure 2b

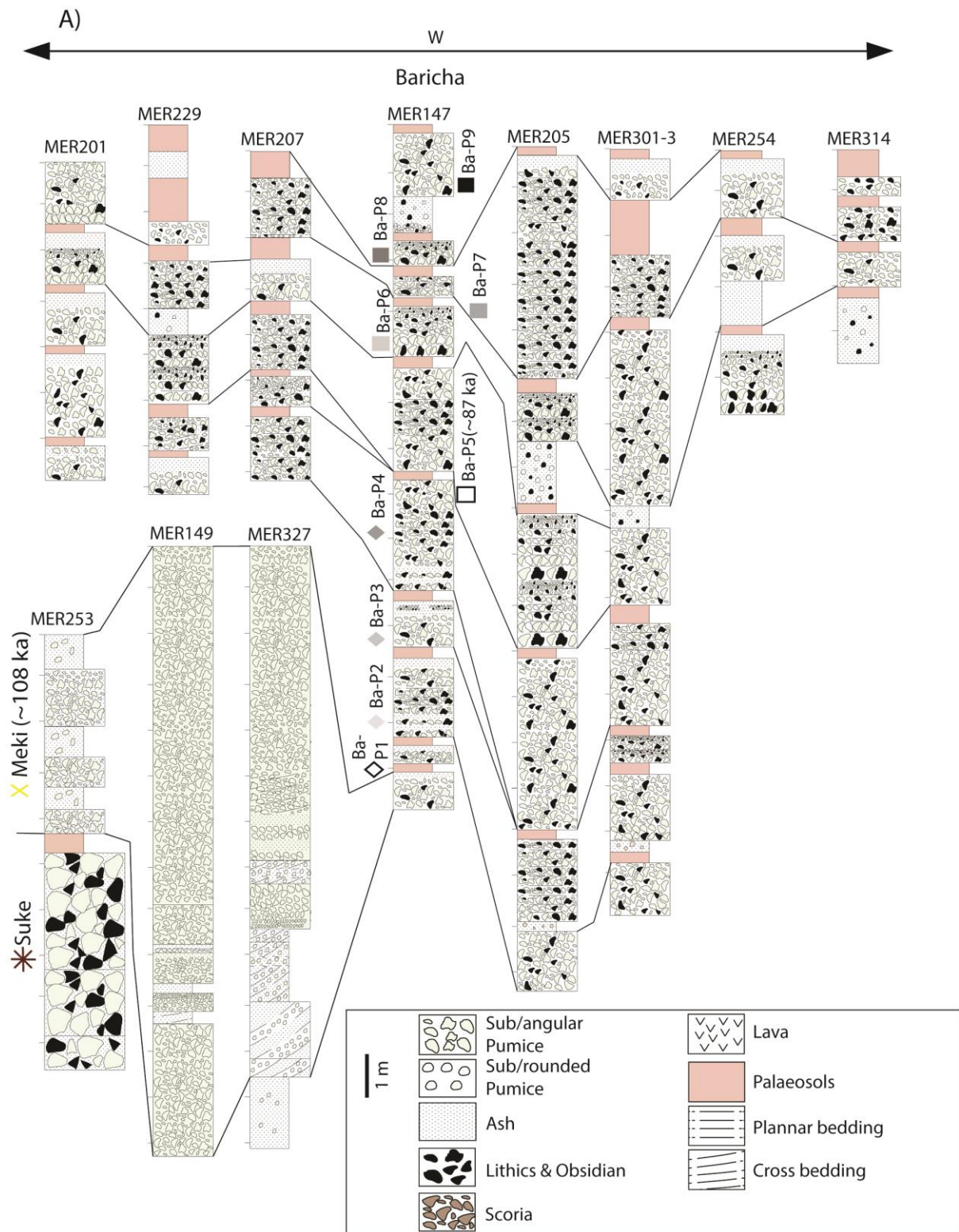


Figure 3a

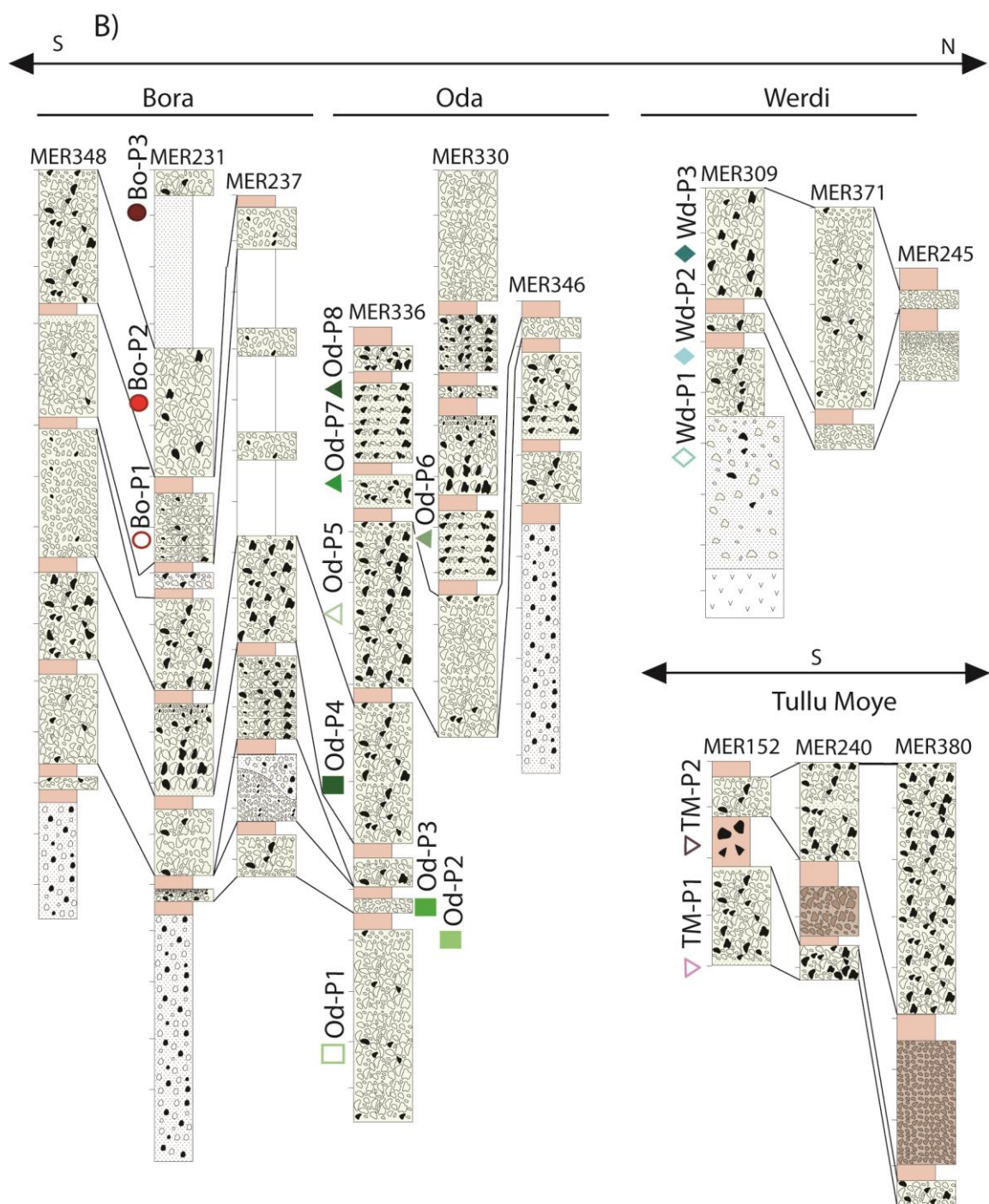


Figure 3b

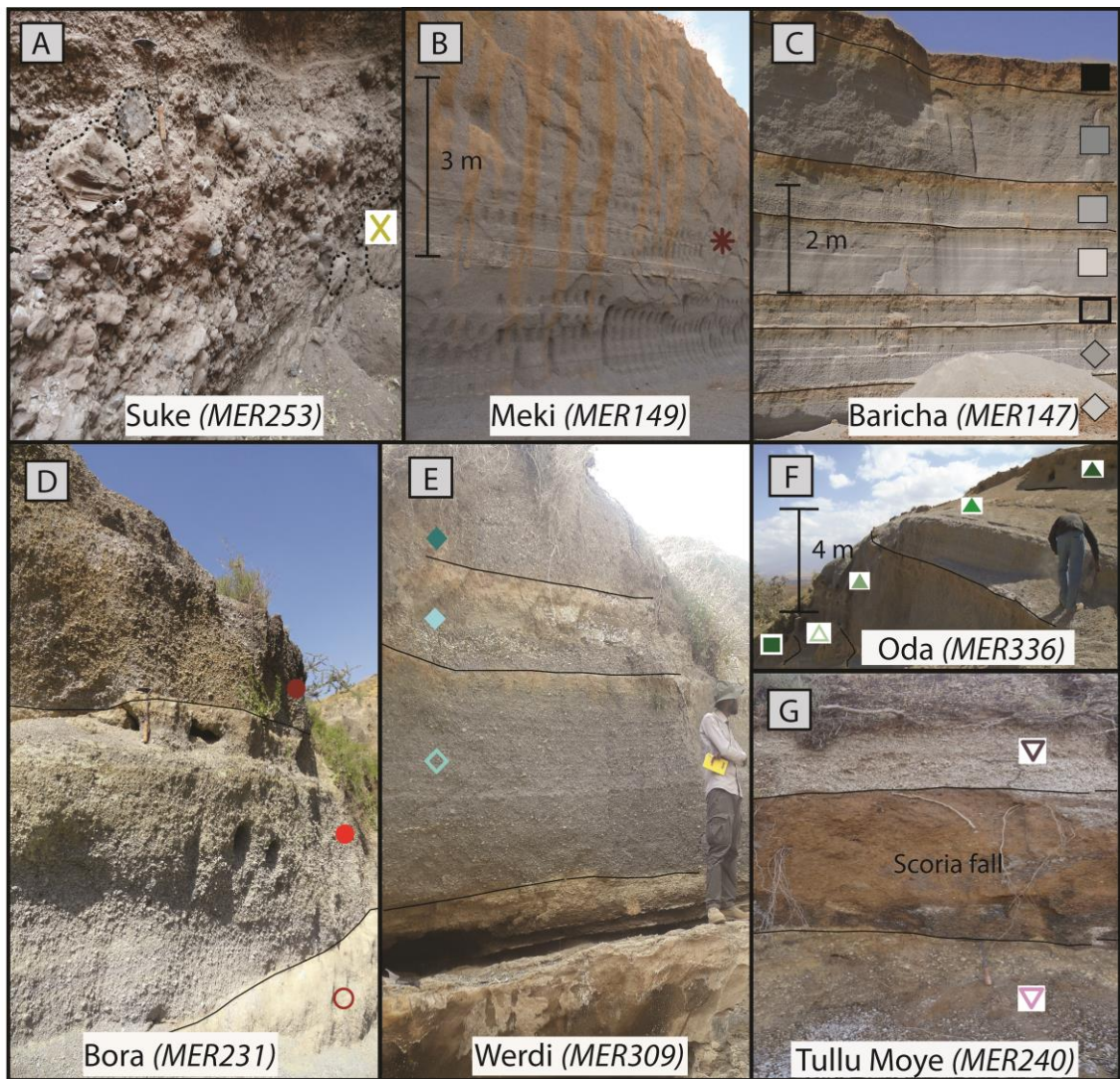


Figure 4

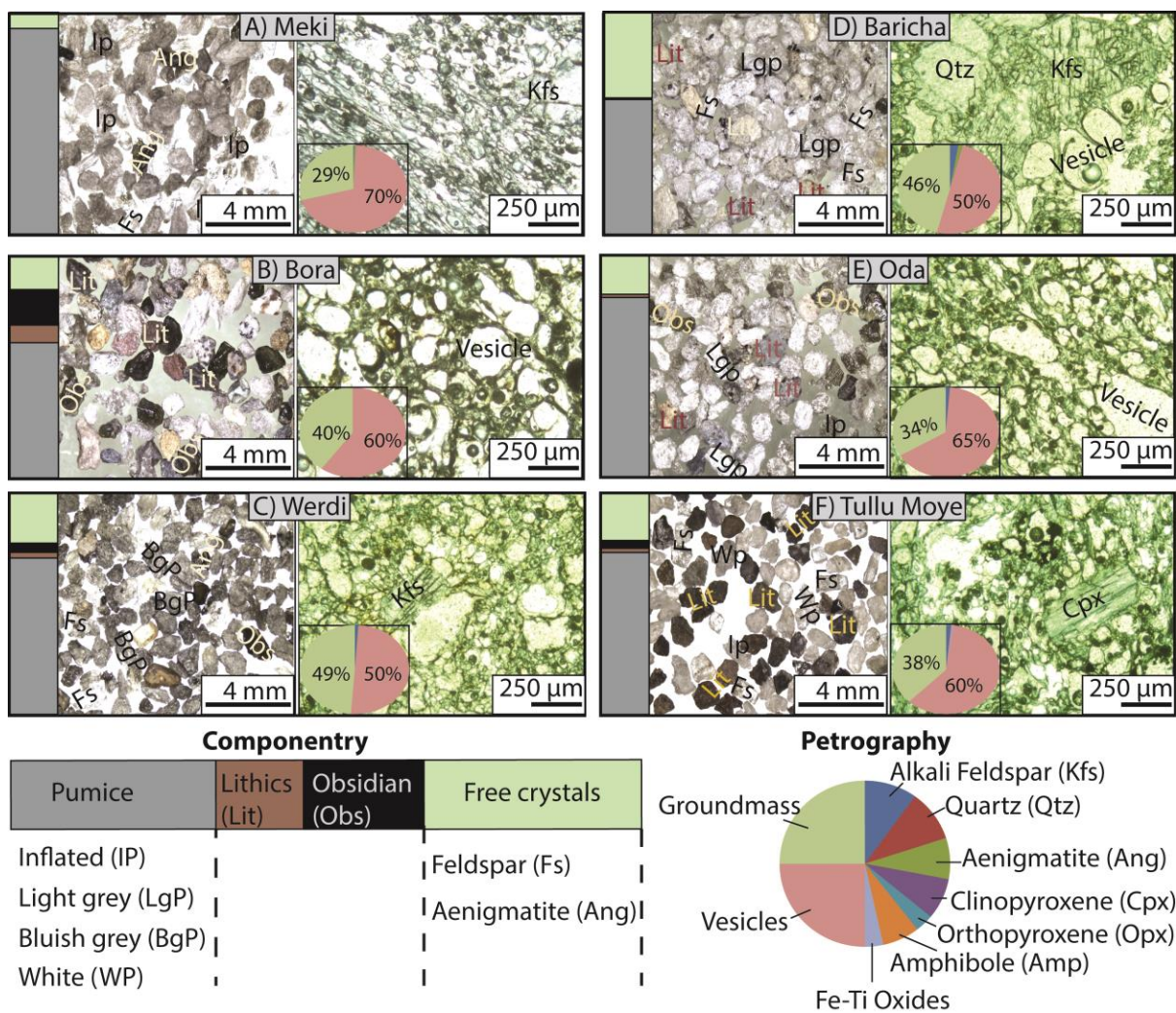


Figure 5

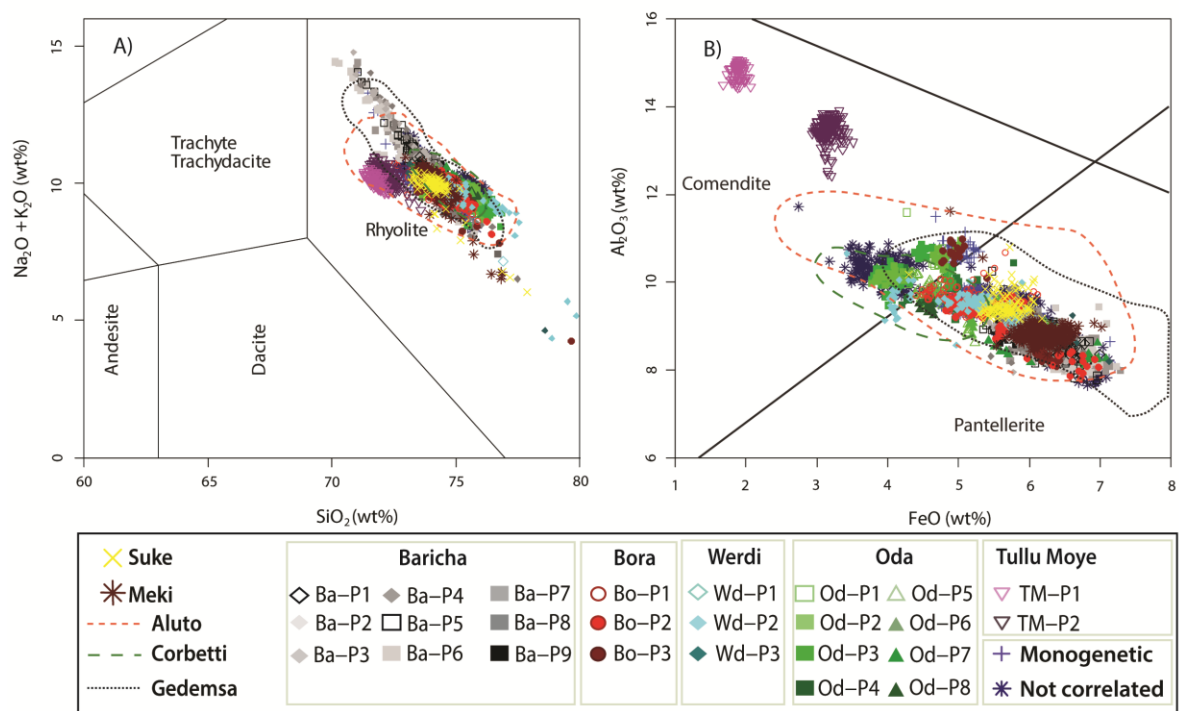


Figure 6

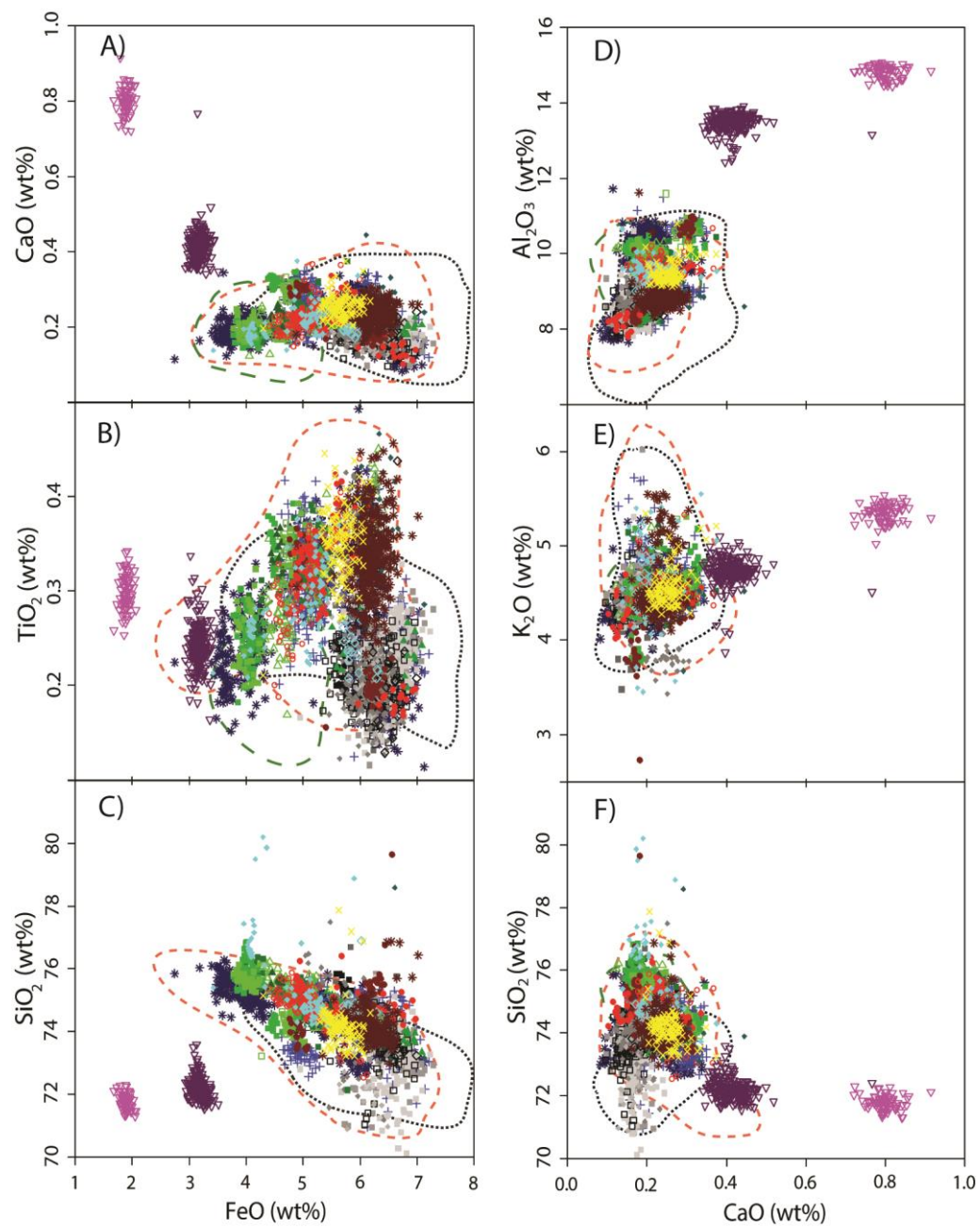


Figure 7

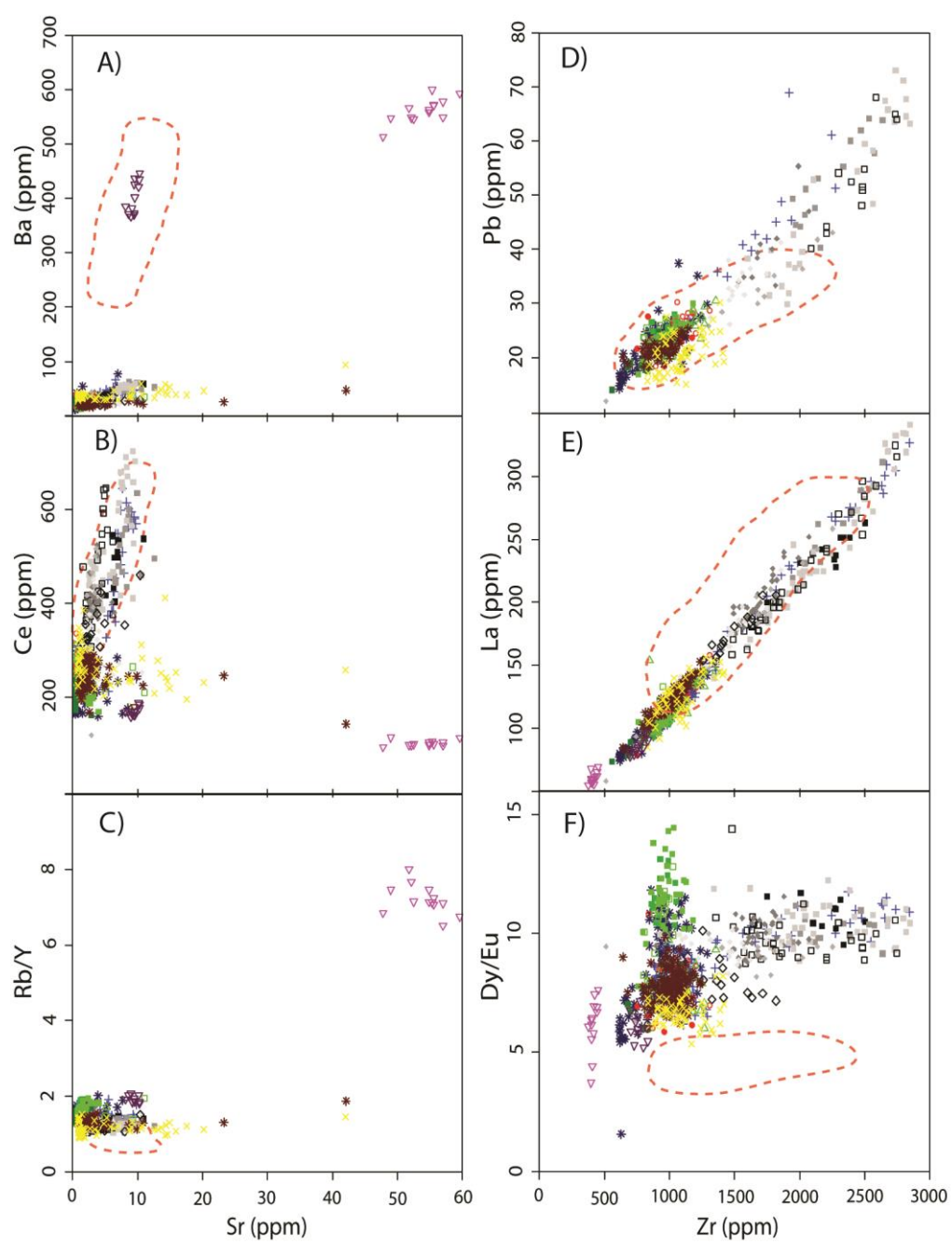


Figure 8

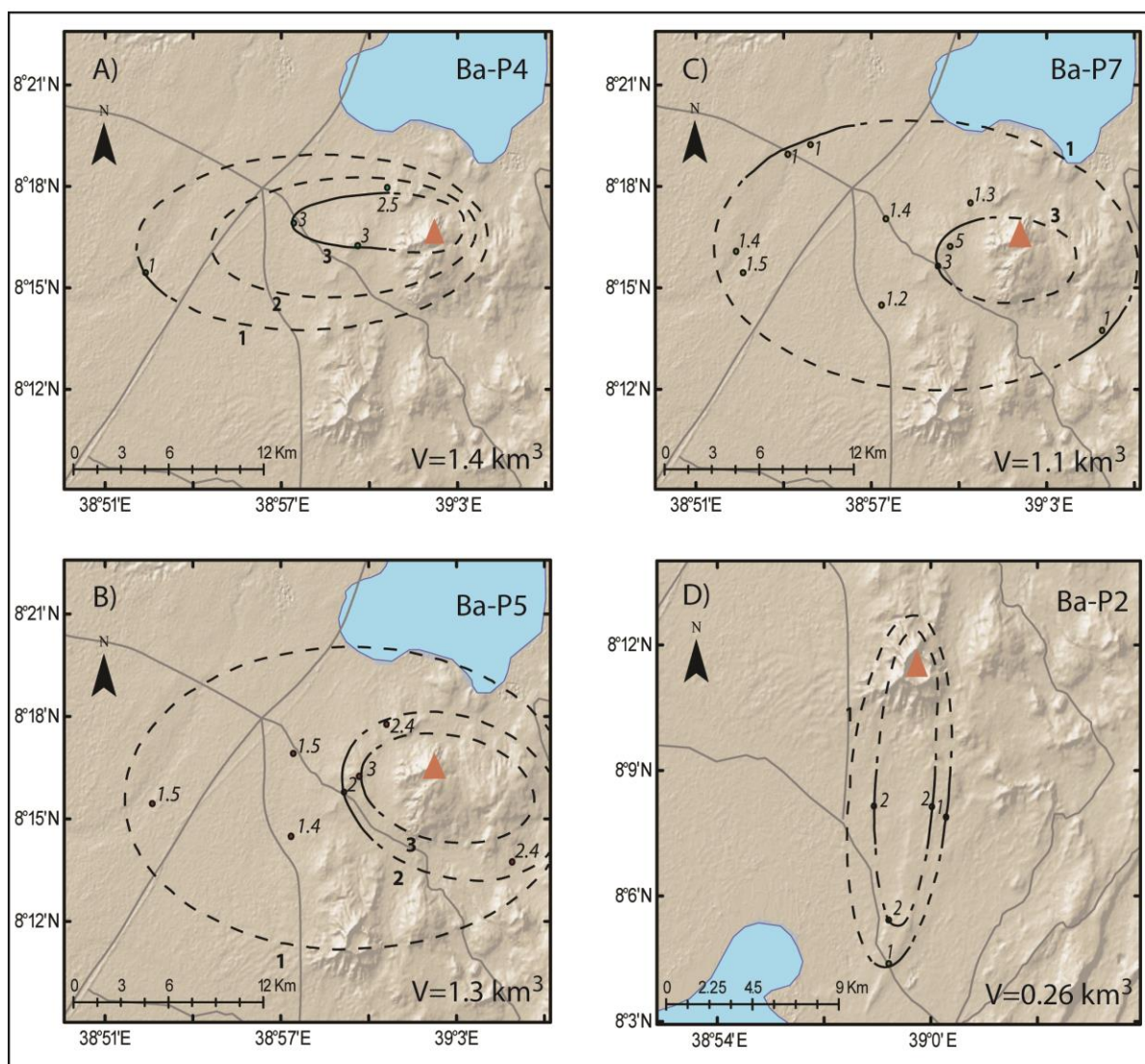


Figure 9

Table 1

Volcanic centre	Sample code	Location		Rock type	Method	Age	Additional note
		Lat	Long				
Unknown	BT-108	Unknown		Obsidian lava	K-Ar	1.58 ± 0.2 Ma	WoldeGabriel et al. (1990)
BBTM	MER149A	8.19	38.85	Tephra	⁴⁰ Ar/ ³⁹ Ar (sanidine)	107.7 ± 8.8 ka	This study
Baricha	MER147-2D	8.29	39	Tephra	⁴⁰ Ar/ ³⁹ Ar (sanidine)	87 ± 16 ka	This study
Baricha	MER308	8.23	39.02	Tephra	¹⁴ C (charcoal)	1190 ± 36 cal yrs BP	This study

Table 2

Source	Unit	Age	Deposit appearance	Interpretation	Componentry (average of grain size fraction <4 mm unless otherwise indicated)	Petrography	Glass composition	Magnitude
BBTM	Suke		Max. Th: 6 m, very poorly sorted, clast-supported, contains bombs and blocks (max. 1 m)	PDC (ignimbrite/lag breccia)	Microvesicular pumice Lava and glassy obsidian lithics	<1% (Ang)	Pantellerite	Caldera forming
BBTM	Meki	108±8 ka	Max. Th: >20 m. Top and bottom is massive, well-sorted pumice lapilli breccia with expanded pumice. The middle part is an alternation of poorly and well sorted pumice lapilli breccia beds. The poorly sorted layers have no consistent local thickness, and show mm-scale low-angle cross bedding, and sub-horizontal laminations of poorly sorted and sub-rounded pumice lapilli in fine ash	Sequence of tephra fall (bottom), PDC (middle) and tephra fall (top)	45-90% microvesicular & ≤40% expanded pumice 5-20% free crystals (Fs & Ang) No lithics	70-75% vesicles <1% phenocrysts (Kfs, Ang) Microlite-poor groundmass	Pantellerite	Caldera forming
Baricha	Ba-P1		Max. Th: 37 cm. Crudely bedded, well sorted and poorly preserved pumice lapilli	Tephra fall	100% microvesicular pumice		Pantellerite	

Ba-P2		breccia Max. Th: 185 cm. Sub-parallel to low angle cross-bedded units of medium ash and crystal-rich lapilli in bottom third. Dm-scale bedded, well sorted lapilli breccia in the middle and upper portions.	PDC; Tephra fall	60% microvesicular & 2% expanded pumice 30% free crystals (Fs/Qtz, Ang/Amp/Px) 5% lithics (lava & glassy obsidian)		Pantellerite	
Ba-P3		Max. Th: 3 m. Bottom 5-10 cm is fine indurated ash with accretionary lapilli. The rest is light grey pumice lapilli breccia, well sorted, massive to cm-scale crudely bedded with occasional pumice bombs (~15 cm)	Tephra fall	80-90% microvesicular pumice ≤20% free crystals (Fs, Ang & Px) <1% crystal-rich obsidian	65% vesicles 6% phenocrysts (Kfs, Ang, Opx) Glassy groundmass	Pantellerite	4.1
Ba-P4		Max. Th: 2.5 m. Cm-scale fine pumice lapilli interbedded with yellowish ash beds at the base. Massive well-sorted pumice lapilli breccia with occasional pumice bombs	Tephra fall	45-75% microvesicular, <5% expanded & ≤1% tube pumice 10-35% free crystals (Fs, Ang & Fe-Ti Oxides) ≤10% lithics (crystal-rich obsidian, lava & ignimbrite)	65% vesicles <1% phenocrysts (Kfs, Ang) microlite-poor groundmass	Pantellerite	5.1
Ba-P5	87 ± 16 ka	Max. Th: 2.5 m. Massive to cm-to-dm scale crudely bedded well-sorted pumice lapilli breccia	Tephra fall	55-75% microvesicular, ≤20% expanded & ≤1% tube pumice 5-40% free crystals (Fs, Ang/Px/Amp & Fe-Ti Oxides)	50-65% vesicles <10% phenocrysts (Kfs, Ang, Amp, Opx)	Pantellerite	5.1

				≤5% lithics (crystal-rich obsidian, lava & ignimbrite) ≤15% obsidian	Glassy groundmass		
Ba-P6		Max. Th: 4 m. Multiple horizons of normally graded and well-sorted pumice lapilli breccia	Tephra fall	50-70% microvesicular & <10% expanded pumice 30% free crystals (Fs, Ang/Amp & Fe-Ti Oxides) ≤2% lithics (crystal-rich obsidian, lava & ignimbrite) ≤5% obsidian	50% vesicles <10% phenocrysts (Kfs, Ang, Amp) Glassy groundmass	Pantellerite	4.8
Ba-P7		Max. Th: 5 m. Dm-scale crudely bedded, overall normally graded, and poorly sorted pumice lapilli breccia with some pumice bombs (10-15 cm)	Tephra fall	65-85% microvesicular, ≤2% expanded & ≤2% tube pumice 5-30% free crystals (Fs, Ang & Fe-Ti Oxides) ≤2% lithics (crystal rich obsidian, lava & ignimbrite) ≤10% glassy obsidian	50-55% vesicles <1% phenocrysts (Kfs & Ang) Glassy groundmass	Pantellerite	5
Ba-P8		Max. Th: 80 cm. Poorly preserved, highly altered orange-stained pumice lapilli breccia, well sorted with diffuse normal grading	Tephra fall	75% microvesicular & <5% expanded pumice <20% free crystals (Fs, Ang) <5% crystal-rich obsidian lithics	65% vesicles 6% phenocrysts (Kfs & Ang) Glassy groundmass	Pantellerite	
Ba-P9	1190 ± 36 cal yr BP	Max. Th: 2.5 m. Cream-coloured, matrix-supported and undulated beds in the	PDC; Tephra fall	80-100% microvesicular <20% free crystals (Fs/Qtz, Ang/Amp/Px)		Pantellerite	

		bottom half. Parallel bedded, well-sorted pumice lapilli breccia at the top		<1% crystal-rich obsidian			
Oda	Od-P1	Max. Th: 4 m. Massive to crudely bedded, poorly sorted pumice lapilli breccia with occasional pumice bombs (3.5 cm)	Tephra fall	100% microvesicular	50% vesicles <3% phenocrysts (Kfs, Ang & Cpx) Glassy groundmass	Pantellerite-Comendite	
	Od-P2	Max. Th: 30 cm. Poorly sorted coarse pumice lapilli breccia with massive to diffuse normal grading	Tephra fall	75-80% microvesicular, 1% tube & ≤1% expanded pumice ≤10% free crystals (Fs/Qtz & Fe-Ti oxides) ≤2% lithics (hydr. altered lava, glassy obsidian & ignimbrite) ≤10% obsidian		Pantellerite-Comendite	
	Od-P3	Max. Th: 2 m. Massive, poorly sorted coarse to fine pumice lapilli breccia	Tephra fall	80% microvesicular & 1% tube pumice ≤5% free crystals (Fs, Ang/Px/Amp & Fe-Ti oxides) ≤3% lithics (hydr. altered lava, glassy obsidian & ignimbrite) ≤10% obsidian	60% vesicles No phenocrysts Glassy groundmass	Pantellerite-Comendite	
	Od-P4	Max. Th: 3 m. Cm-scale bedded, each bed set is normally graded pumice lapilli	Tephra fall; PDC	60-80% microvesicular & ≤1% tube pumice 10-20% free crystals (Fs,	55-65% vesicles ≤3%	Pantellerite-Comendite	4.7

	breccia underlain by a lithic-rich poorly sorted ash horizon		Ang, Amp, Px & Fe-Ti oxides) ≤25% lithics (hydr. altered lava, glassy obsidian & ignimbrite)	phenocrysts (Kfs, Cpx, Amp, Ang) Glassy to microlite-poor groundmass	
Od-P5	Max. Th: 3.5 m. Massive and poorly-sorted pumice lapilli breccia with occasional distinct bigger clasts (3.5 cm)	Tephra fall	60-70% microvesicular & ≤1% tube pumice 5-35% free crystals (Fs/Qtz, Ang/Px/Amp & Fe-Ti oxides) ≤3% lithics (hydr. altered lava & glassy obsidian) <25% obsidian		Pantellerite-Comendite 4.6
Od-P6	Max. Th: 90 cm. Main unit is massive poorly sorted pumice lapilli breccia. Its top and bottom are marked by thin ash beds (10-20 cm)	Tephra fall	95% microvesicular pumice 5% lithics (lava & glassy obsidian)		Pantellerite-Comendite
Od-P7	Max. Th: 16 m. Interbedded horizons of coarse ash and rounded fine pumice lapilli, lenticular bedding, well sorted within each bed but deposit is poorly sorted overall	PDC	70% microvesicular pumice <25% free crystals (Fs/Qtz & Fe-Ti oxides) 1% lithics (hydr. altered lava, glassy obsidian & ignimbrite) <5% obsidian		Pantellerite-Comendite
Od-P8	Max. Th: 1.85 m. Well-sorted coarse pumice lapilli breccia with subtle normal grading	Tephra fall	90% microvesicular & 1% expanded pumice 5% lithics (lava, glassy		Pantellerite-Comendite

Bora	Bo-P1	Max. Th: 1 m. Dm-scale crudely bedded, well-sorted pumice lapilli breccia; top few centimetres shows interbedding of coarse ash and pumice lapilli	Tephra fall	obsidian & ignimbrite) 80% microvesicular, 5% expanded & 1% tube pumice <10% free crystals (Fs/Qtz & Fe-Ti oxides) 5% obsidian and lithics (lava, glassy obsidian & ignimbrite)		Pantellerite-Comendite	
	Bo-P2	Max. Th: 2.5 m. Cm-scale bedded, well-sorted pumice lapilli breccia with occasional pumice bombs (15 cm)	Tephra fall	60% microvesicular pumice ≤15% free crystals (Fs/Qtz & Fe-Ti oxides) <8% (hydr. altered lava, glassy obsidian & ignimbrite) 15% obsidian	60% vesicles No phenocrysts Glassy groundmass	Pantellerite-Comendite	4.3
	Bo-P3	Max. Th: >3 m. Massive, poorly to well-sorted coarse pumice lapilli breccia	Tephra fall	80% microvesicular, 5% expanded & 3% tube pumice 5% free crystals (Fs, Ang, Px & Fe-Ti oxides) ≤1% lithics (altered lava, glassy obsidian) 5% obsidian	45% vesicles <0.5% phenocrysts (Kfs & Opx) Microlite-poor groundmass	Pantellerite	4.2
Wardi	Wd-P1	Max. Th: >15 m. Cm-scale bedded, poorly sorted, coarse ash to medium sized bluish-grey pumice lapilli breccia	Tephra fall	83% microvesicular pumice 5% free crystals (Fs/Qtz, Ang/Px/Amp) 10% lithics (hydr. altered		Pantellerite-Comendite	4.6

				lava & crystal-rich obsidian)			
	Wd-P2	Max. Th: 35 cm. Massive, well-sorted, bluish-grey pumice lapilli breccia	Tephra fall	70% microvesicular pumice 20% free crystals (Fs, Ang & Fe-Ti oxides) <5% lithics (hydr. altered lava, glassy obsidian & ignimbrite) <5% obsidian	50% vesicles 1% phenocrysts (Kfs & Ang) Glassy groundmass	Pantellerite-Comendite	4.4
	Wd-P3	Max. Th: 2.1 m. Massive, poorly sorted, bluish-grey coarse pumice lapilli breccia	Tephra fall	<85% microvesicular pumice <10% free crystals (Fs/Qtz, Ang/Px/Amp) <10% lithics (hydr. altered lava, glassy obsidian & ignimbrite)		Pantellerite-Comendite	
Tullu Moya	TM-P1	Max. Th: 3 m. Massive, poorly sorted, white pumice lapilli breccia	Tephra fall	80-85% microvesicular, ≤2% expanded & <5% tube pumice ≤10% free crystals (Fs/Qtz, Px/Amp & Fe-Ti oxides) <10% lithics (hydr. altered lava & glassy obsidian)		Comendite	
	TM-P2	Max. Th: 2 m. Massive, poorly sorted, white pumice lapilli	Tephra fall	70-100% microvesicular, ≤1% expanded and ≤1%	60% vesicles 2%	Comendite	2.8

breccia containing occasional
pumice bombs (15 cm)

tube pumice
≤20% free crystals (Fs,
Px/Amp & Fe-Ti oxides)
<3% (hydr. altered lava &
glassy obsidian)
<5% glassy obsidian

phenocrysts
(Kfs, Cpx, Amp
& Fe-Ti oxide)
Glassy
groundmass

Table 3

Group Unit Sample (MER)	Suke	Meki	Baricha								
			Ba-P1	Ba-P2	Ba-P3	Ba-P4	Ba-P5	Ba-P6	Ba-P7	Ba-P8	Ba-P9
Major	253-1D	149B	147-4F	205-2E	205-2C	147-2F	147-2A	147-1E	205-1B	147-1C	147-1A
Trace	n=27	n=30	n=21	n=26	n=26	n=30	n=29	n=24	n=24	n=29	n=12
	N=14	N=15	N=14	N=15	N=10	N=9	N=11	N=15	N=14		N=11
SiO ₂	73.92(0.6)	74.08(0.3)	73.65(0.2)	73.91(0.6)	73.36(1.2)	74.03(0.2)	74.54(0.3)	74.01(0.4)	73.12(1.0)	73.75(0.3)	73.97(0.2)
TiO ₂	0.36(0.1)	0.33(0.0)	0.22(0.1)	0.22(0.0)	0.22(0.0)	0.19(0.0)	0.23(0.0)	0.18(0.0)	0.21(0.0)	0.20(0.0)	0.21(0.0)
Al ₂ O ₃	9.83(0.4)	8.72(0.1)	8.51(0.2)	9.04(0.2)	8.45(0.4)	8.57(0.1)	8.94(0.1)	8.74(0.4)	8.43(0.1)	8.45(0.1)	8.61(0.1)
FeO	5.65(0.3)	6.10(0.2)	6.51(0.2)	5.80(0.1)	6.12(0.4)	6.30(0.2)	5.77(0.2)	6.08(0.3)	6.25(0.3)	6.36(0.2)	6.21(0.2)
MnO	0.21(0.0)	0.23(0.0)	0.28(0.1)	0.24(0.0)	0.23(0.0)	0.27(0.1)	0.22(0.0)	0.23(0.0)	0.24(0.0)	0.27(0.0)	0.23(0.0)
MgO	0.01(0.0)	0.01(0.0)	0.01(0.0)	0.02(0.0)	0.01(0.0)	0.01(0.0)	0.01(0.0)	0.01(0.0)	0.00(0.0)	0.01(0.0)	0.01(0.0)
CaO	0.28(0.0)	0.23(0.0)	0.21(0.0)	0.20(0.0)	0.17(0.0)	0.18(0.0)	0.20(0.0)	0.17(0.0)	0.16(0.0)	0.16(0.0)	0.17(0.0)
Na ₂ O	4.97(0.7)	5.87(0.2)	6.22(0.2)	6.0(0.7)	7.00(1.5)	6.0(0.2)	5.62(0.1)	6.08(0.3)	7.14(1.2)	6.34(0.2)	6.17(0.2)
K ₂ O	4.74(0.3)	4.4(0.1)	4.39(0.1)	4.55(0.1)	4.43(0.2)	4.45(0.1)	4.47(0.1)	4.49(0.2)	4.43(0.1)	4.45(0.1)	4.42(0.1)
Rb	118	129	187	151	198	217	200	250	282		284
Sr	11	2	4	4	3	3	3	3	8		7
Y	100	100	154	119	168	176	167	200	220		207
Zr	1105	876	1443	1116	1653	1597	1664	2018	2240		2219
Nb	149	138	225	169	246	266	255	313	318		315

Cs	1	2	2	2	2	3	2	3	4	4
Ba	46	19	23	21	26	20	23	24	51	46
La	114	112	170	134	187	188	180	216	255	239
Ce	246	225	344	273	383	390	364	452	519	488
Nd	107	101	151	119	159	179	157	190	217	195
Sm	23	20	32	25	33	34	32	38	42	39
Eu	3	3	4	3	3	3	3	3	4	4
Gd	19	19	28	21	27	31	29	36	37	36
Dy	20	19	31	22	29	34	31	37	40	39
Yb	12	11	16	12	17	19	18	22	23	24
Hf	25	21	36	26	34	40	38	47	52	53
Ta	10	8	15	10	13	16	15	18	20	20
Th	20	17	27	21	28	31	29	35	42	40
U	4	4	7	5	6	8	7	9	11	10

Table 3 continued

Group	Werdi						Oda				
Unit	Wd-P1	Wd-P2	Wd-P3	Od-P1	Od-P2	Od- P3	Od-P4	Od-P5	Od-P6	Od-P7	Od-P8
Sample (MER)	368B n=18	155B n=28	155A n=23	336I n=19	336H n=17	336G n=28	336F n=18	336D n=14	336C n=18	330B n=16	336A n=19
SiO ₂	74.79(0.6)	74.76(0.9)	74.03(1.1)	74.18(0.4)	74.11(0.4)	74.34(0.3)	75.11(0.4)	75.24(0.4)	74.90(0.4)	74.27(0.6)	75.14(0.5)
TiO ₂)))))))))))
	0.24(0.0)	0.31(0.0)	0.37(0.1)	0.34(0.0)	0.35(0.0)	0.35(0.0)	0.33(0.0)	0.31(0.0)	0.34(0.0)	0.24(0.0)	0.34(0.0)
				10.60(0.3)	10.58(0.2)	10.49(0.3)					
Al ₂ O ₃	8.94(0.2)	9.57(0.1)	8.82(0.2))))	9.72(0.3)	9.20(0.3)	9.30(0.3)	8.34(0.2)	9.42(0.1)
FeO	5.93(0.2)	5.23(0.3)	6.29(0.3)	4.71(0.1)	4.82(0.1)	4.62(0.2)	4.96(0.1)	5.23(0.1)	5.29(0.1)	6.35(0.7)	5.00(0.5)
MnO	0.23(0.0)	0.20(0.0)	0.24(0.1)	0.19(0.0)	0.19(0.0)	0.19(0.0)	0.19(0.0)	0.21(0.0)	0.21(0.0)	0.28(0.0)	0.21(0.0)
MgO	0.02(0.0)	0.01(0.0)	0.01(0.0)	0.02(0.0)	0.01(0.0)	0.01(0.0)	0.01(0.0)	0.01(0.0)	0.01(0.0)	0.01(0.0)	0.01(0.0)
CaO	0.2(0.0)	0.24(0.0)	0.28(0.1)	0.29(0.0)	0.30(0.0)	0.32(0.0)	0.24(0.0)	0.21(0.0)	0.22(0.0)	0.21(0.0)	0.23(0.0)
Na ₂ O	4.90(0.8)	5.04(0.9)	5.53(1.0)	5.08(0.2)	5.02(0.2)	4.99(0.4)	4.90(0.2)	5.16(0.1)	5.24(0.2)	5.79(0.3)	5.11(0.2)

K ₂ O	4.76(0.3)	4.61(0.4)	4.42(0.2)	4.59(0.2)	4.60(0.2)	4.67(0.2)	4.53(0.2)	4.44(0.1)	4.48(0.2)	4.51(0.1)	4.52(0.2)
------------------	-----------	-----------	-----------	-----------	-----------	-----------	-----------	-----------	-----------	-----------	-----------

Table 3 continued

Group	Bora			Tullu Moye	
Unit	Bo-P1	Bo-P2	Bo-P3	TM-P1	TM-P2
Sample					
(MER)	231D	231B	230A	152A	152B
	n=28	n=30	n=28	n=24	n=24
	N=	N=15		N=12	N=13
SiO ₂	74.08(0.8)	74.65(0.2)	75.40(1.0)	72.06(0.2)	71.74(0.2)
TiO ₂)))))
	0.34(0.0)	0.32(0.0)	0.20(0.0)	0.24(0.0)	0.30(0.0)
				13.28(0.1)	14.60(0.1)
Al ₂ O ₃	9.46(0.2)	9.36(0.1)	8.43(0.4)))
FeO	5.43(0.4)	5.18(0.1)	6.22(0.2)	3.17(0.2)	1.89(0.1)
MnO	0.21(0.1)	0.19(0.0)	0.24(0.0)	0.15(0.0)	0.07(0.0)
MgO	0.01(0.0)	0.01(0.0)	0.01(0.0)	0.08(0.0)	0.24(0.0)
CaO	0.24(0.0)	0.22(0.0)	0.17(0.0)	0.41(0.0)	0.80(0.0)
Na ₂ O	5.74(0.3)	5.64(0.1)	5.37(0.9)	5.85(0.2)	4.93(0.2)
K ₂ O	4.48(0.1)	4.41(0.1)	3.94(0.4)	4.74(0.1)	5.37(0.1)
Rb	159	147		126	171
Sr	1	1		9	54
Y	105	98		66	24
Zr	984	977		766	415
Nb	166	150		112	66
Cs	2	2		1	2
Ba	28	25		401	562
La	120	112		85	60
Ce	254	235		172	103
Nd	109	101		72	31
Sm	21	20		13	5

Eu	3	3	2	1
Gd	18	18	12	4
Dy	19	18	12	4
Yb	11	11	8	3
Hf	24	22	18	10
Ta	10	9	7	5
Th	21	20	17	24
U	5	5	4	6
